April 2009

Polymer Brush Force Modeling and Experimentation

Evan Vincent Anderson
Worcester Polytechnic Institute

Repository Citation

Anderson, E. V. (2009). *Polymer Brush Force Modeling and Experimentation*. Retrieved from https://digitalcommons.wpi.edu/mqp-all/278

Project Number: PH-NAB-MP10

POLYMER BRUSH FORCE MODELING AND EXPERIMENTATION

A Major Qualifying Project Report:

Submitted to the Faculty

of the

WORCESTER POLYTECHNIC INSTITUTE

in partial fulfillment of the requirements for the

Degree of Bachelor of Science

by

x________________________________

Evan Anderson

Date: April 30, 2009

Approved:

x________________________________

Professor Nancy Burnham, Major Advisor

1. Atomic Force Microscopy
2. Bacterial Adhesion
3. Biofilms

x________________________________

Professor Terri Camesano, Co-Advisor

Table of Contents

I – List of Tables and Figures

II – Abstract

Atomic force microscope (AFM) force measurements were taken on an alginate-polymer brush in varying pH buffer solutions in order to determine the meaning of the variable *s* in the force model. The current understanding is that *s* is the root spacing of the polymers, but this experiment suggests that *s* is the mesh spacing. The force curves were fit in order to determine the brush parameters. It was found that all parameters increased as a function of pH.

III – Acknowledgements

There are several people who deserve acknowledgement for the progress made on this project, but the first one who needs my personal thanks is Paola Pinzon, a PhD BME student at Gateway Park. She trained me to use their AFM, and worked side-by-side with me for the majority of the experiments. She even assisted with the data processing and helped me to revise some of the chapters in this report. Without her, we would not have been so successful.

I would like to thank my advisors, Professors Nancy Burnham (Physics) and Terri Camesano (Chemical Engineering). Their guidance and support helped to keep me on track with the short amount of time we had to conduct and interpret the experiment. Professor Burnham is an AFM expert, but also derived the force models used to fit our experimental data. She was also the one who proposed this project and initially exposed the weakness in other groups' interpretations of *s*. Terri Camesano is an expert in bacterial and colloidal interactions. She provided the missing chemical engineering knowledge that enabled some of the more technical aspects of the experiment. She also has extensive experience with AFM and the forces involved with bacteria. Both of my advisors played a central role in providing feedback on my report as it has developed, and I would like to thank them both for that.

I would also like to thank Ray Emerson and Adriana Hera for the Matlab coding that was necessary to process the data obtained from the AFM. Ray Emerson was a PhD Chemical Engineering student who originally wrote the code. Adriana Hera is the Matlab expert here at WPI. She helped me attempt to modify Ray's code, and even to write some of my own. She also helped me try to fit our data in Matlab, and with a little bit more time it probably would've worked.

I would like to thank all of you. I really appreciate your help and guidance throughout this project.

IV – Executive Summary

This project is an investigation of the interaction forces involved between the tip of an atomic force microscope and an alginate-polymer brush. The polymer brush was used to replicate the pili on the surface of bacteria. The purpose of this type of research is to explore how bacteria adhere and form biofilms, so that their formation may be prevented. Biofilms are responsible for over half of infections in the Western Hemisphere and billions of dollars in damages every year to industrial machinery and plumbing.

The experimental part of this project attempts to investigate the current interpretation of the parameter *s* in the force interaction model of a polymer brush. It is believed by many that this variable is the spacing between roots in the polymer brush, but the hypothesis of this project is that it is instead the mesh spacing, or the average distance between polymer overlaps.

The polymer brush conformation can be manipulated by varying the pH buffer that it is submerged in—the polymers relax in high pH and constrict in low pH. Force measurements are taken in each of these conditions and the brush parameters are obtained from fitting the experimental data. If the value for *s* does not change between these conditions, then the root spacing hypothesis would be verified by this experiment. Conversely, if *s* does change with pH, the mesh spacing hypothesis would be supported.

The results seemed to substantiate our hypothesis: that *s* is indeed the mesh spacing instead of the root spacing. It was found that *s* varied from 90 to 100 nm across three pH buffer solutions (5.5, 6, and 7). Although its value did not change much, it did change with pH which would negate the root spacing theory—root spacing should be invariant regardless of brush conformation. This has substantial implications in this research field because *s* has been interpreted as the root spacing for many years. The results of this particular experiment are not considerably trustworthy because the experiment never made it to a quantitative stage due to time constraints. The results do suggest that more research needs to be done, and some prospects are explored at the end of this report. [5]

1 Introduction

This report is structured as follows: introduction, literature review, experimental, and finally results and discussion. The literature provides the necessary background information needed to properly understand the experiment and purpose. The literature review discusses biofilms, bacterial adhesion, force models, atomic force microscopy (AFM), polymer physics, and surface properties in a level of detail that will enable full comprehension of the experiment. The experimental chapter discusses materials and methods used to conduct the experiment and the experiment itself. The results chapter contains the results of the experiment and an interpretation of their meaning and implications which are summarized in the conclusion. This chapter also contains a section regarding possible improvements to be made to the experiment that should be considered for further research. A brief overview of the experiment and its background will now be given.

This experiment is an AFM investigation of the interaction force between the AFM tip and a polymer brush. The purpose of this type of research is to obtain a better understanding of how bacteria interact to form biofilms, so that their formation can be prevented. Biofilms are responsible billions of dollars in losses each year from infection and biofouling in the industry [3], so their prevention is of great interest in these fields.

Biofilms are colonies of microorganisms that are responsible for 65% of infections in the Western Hemisphere [6]. They constitute over half of the Earth's biomass [3], and 99% of bacteria reside in biofilms. This presents a problem because antibiotics are typically developed to combat planktonic or individual bacteria, but biofilms are resistant to doses of up to one-thousand times of what would kill an equal amount of planktonic cells [3]. There is no completely effective way to remove a biofilm, and for this reason it is important to attempt to prevent their formation altogether. Biofilms will be discussed in greater detail in the next chapter, the literature review.

This experiment attempts to investigate the general interpretation of a certain parameter, *s*, in the force model for the interaction between an AFM tip and a polymer brush. The variable seems to act as a density and the prevailing belief is that it corresponds to the spacing between the roots of the polymers in the brush. We believe it would be more logical that it correspond to mesh spacing, or the distance between regions where polymers overlap. A thought experiment can be performed to illustrate this point: Imagine rowing in a marsh and wondering how deep it was. One would be able to measure the depth of the marsh by sticking one's paddle into the water and observing how far down the oar went until it could no longer be pushed further. If the vegetation in the marsh is dense enough, one might assume that the density observed by the oar would be a consequence of the overlapping of weeds instead of simply the spacing between their roots. We believe this thought experiment is analogous to the interactions between the AFM tip and the polymer brush and that a mesh spacing theory is more sensible.

The experiment attempts to determine the true meaning of *s* by manipulating the conformation of the polymer brush, and fitting the experimental data with a derived force model. This would then give parameters for each condition. If *s* is truly the root spacing between polymers, it should be invariant under a conformational change in the brush, and the fitted values for *s* should also be invariant. This is the basis for this project.

A replica was used to simulate the polymers on a bacterium because the elasticity of the bacterium cell wall couples with the force involved with the polymer brush. It is somewhat difficult to decouple these interactions, and the behavior of the polymers themselves is what drives bacterial adhesion. The molecule used to replicate the bacterial brush was alginate, a polymer known to be found in biofilms that cause cystic fibrosis. The alginate is bound to a glass slide and force measurements are then taken using an AFM. A theoretical force model is then fitted to the experimental data to obtain the brush parameters (length, density, etc). The data is then transferred to a semi-log effective density plot to visualize the trends as pH increases, but mostly to see if *s* changes at all. This plot provides an ultimate result that visually depicts the substantiation or negation of the mesh spacing hypothesis.

2 Literature Review

2.1 Introduction to Biofilms

2.1.1 Biofilm Overview

The primary motivation for our study of alginate polymers is an attempt to further our knowledge of the formation and function of biofilms in natural, medical, and industrial contexts. Biofilms form when many individual bacteria or microorganisms assemble on a surface. They are responsible for billions of dollars in losses [3] throughout the world each year by degradation, infection, and maintenance. They are responsible for 65% of all human infection in the western hemisphere [6]. Biofilms are extremely resistant to conventional antibiotics and are very flexible as far as environments they can inhabit. For these reasons they are a common general focus of many studies and experiments.

Figure 2-1 – A biofilm system in a stream. The biofilm is a slippery film that develops on rocks. [1]

Biofilms are, in nature at least, a plethora of different microorganisms that are commonly found attached to surfaces that come in contact with moisture at some point or another. They tend to prefer environments that are wet and rich with nutrients, although, biofilms are incredibly indifferent when it comes to suitable living environments. The most common or well-known biofilm is probably dental plaque where over 500 different microbial species have been identified [3]. Other common examples of biofilms are the slippery films found on pool walls, rocks in streams, the films sometimes seen in puddles or on ponds, soap scum, and the gunk found in drains and pipes.

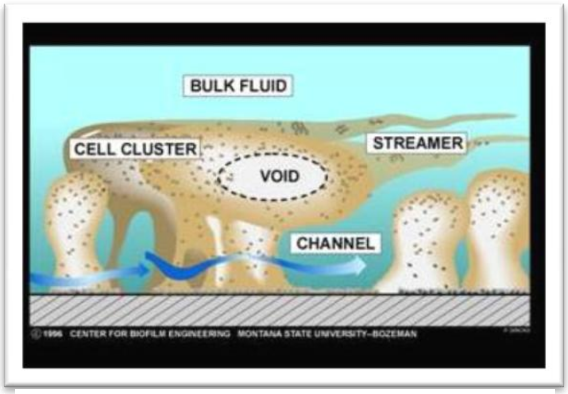

Figure 2-2 – Microscopic view of a biofilm and structural characteristics [3].

Biofilms are typically composed of—but not limited to—bacteria, algae, fungi, yeasts, and protozoa [3] held together by a sugary substance known as extracellular polymeric substance (EPS), exopolysaccharides, or the extracellular matrix (ECM). The EPS creates an environment that easily accommodates several species of microorganisms' attachment and survival. Biofilms can basically be seen as a collective microbial survival mechanism; survival is more probable in a community rather than as an individual. Bacteria that are part of a biofilm are called *sessile* while free-floating bacteria are known as *planktonic*. Over half of the planet's biomass is in biofilms [3] and over 99% of bacteria are sessile—contrary to our stereotypical, planktonic understanding of bacteria. We will see in our discussion of biofilm treatment how this planktonic paradigm has ultimately handicapped us in our fight against infection and disease.

2.1.2 Biofilm Development

There are conventionally five stages of biofilm development: initial attachment, irreversible attachment, maturation I, maturation II, and dispersion [7]. The biofilm is initiated by what is known as a *conditioning film* made up of polysaccharides and/or proteins. The first organism to come into contact with the surface has the ability to secrete this conditioning film, which allows for easier attachment of other organisms and faster growth of the microbial network. The need for this conditioning film pertains to the difficulty for a single microbe to attach to the substrate, but this microscopic difficulty is generally negligible on a macroscopic scale simply because of the number of planktonic microbes incident on an exposed surface.

In the initial attachment phase, the typically negatively-charged planktonic cell becomes subject to the electrostatic repulsion of the substrate (many of which are also negatively charged) [8]. The microbe must have enough kinetic energy to overcome this potential barrier in order to begin to experience attractive van der Waals forces. The kinetic energy used to overcome the repulsive potential may be supplied by the flow of the solution, but it is also hypothesized that the flagella assist the microbe in overcoming the potential barrier. Once the cell comes into contact with the substrate it is temporarily attached by van der Waals forces. The microbe may, however, be swept away by whatever means as long as the means has enough energy to overcome the van der Waals potential. If this does not happen, the initial or "reversible" attachment stage is over because once the microbe adheres to the substrate, biofilm formation is for the most part inevitable. The microbe only needs to be within 5 nm to "permanently" attach to the surface by surface receptors such as pili [9].

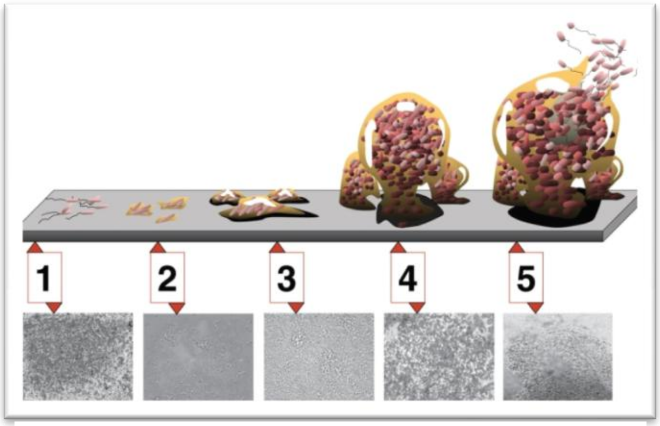

Figure 2-3 – The stages of biofilm development. 1. Initial Attachment. 2. Permanent Attachment. 3. Maturation I 4. Maturation II 5. Dispersion. [2]

The microbe changes drastically after it comes into contact with the surface—20% of the genome is activated and the cell begins secreting polysaccharides and proteins to form the conditioning film [7]. Once the microbe begins secreting the conditioning film it has adhered to the substrate; this is the irreversible attachment stage. During this stage the microbe continues to secrete EPS so other microorganisms more readily attach, skipping initial attachment altogether.

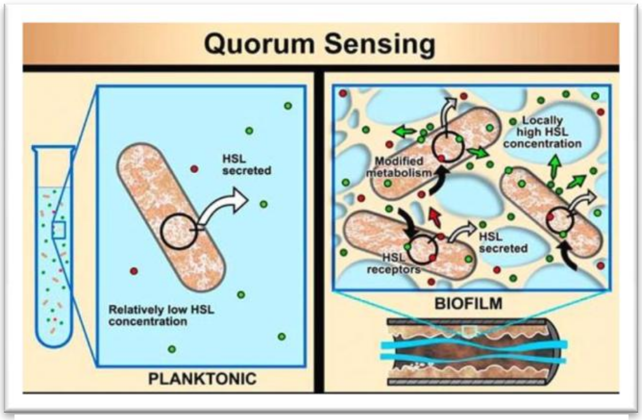

Figure 2-4 – The quorum sensing phenomenon. This refers to how cells can "sense" the presence of others and initiate some function in response [3].

The biofilm now begins to mature. The microbes caught in the extracellular matrix begin to undergo cell division whilst more novel organisms adhere to the film. There is generally no specific sequence to how the biofilm builds and recruits new species in this stage, but it has been shown that some specific systems such as dental plaque actually do have a succession that microbial cells must bind in [10]. Each wave of organisms provides a binding site for the succeeding wave. Incident microbes need not be alive to bind to the ECM, adding to the mass and diversity of the biofilm.

Maturation II is perhaps the most interesting phase in biofilm development. It is in this stage that we first observe the phenomenon known as *quorum sensing*. Quorum sensing is an instance of intracellular communication where microbes within the ECM reach a chemically-activated-quorum and initiate a new function of growth. In Maturation II, this function manifests with the building of mushroom-shaped towers branching out of the original. These structures are incredibly complex in nature, but it has been observed that biofilms generally tend to exhibit this behavior when the substrate has a lower nutrient content, as opposed to colonies that pack tightly around a substrate with high nutritional content [10]. Perhaps the branching out is an attempt to collect nutrients found above the substrate as a method of compensation. The more tightly packed films are, the better they are attached to their surfaces than ones that branch out.

Another instance of quorum sensing occurs in the final stage of biofilm development, dispersion. In dispersion, parts of the microbial-EPS towers begin to appear physically different from the rest of the film. These parts of the towers are packed with both planktonic and sessile microbial progeny and eventually break off from the rest of the ECM to travel (usually downstream) to other surfaces. Dispersion may also be a result of a high turbulent flow, effectively physically detaching parts of the biofilm and moving them downstream. This can be seen in pipe systems and is sometimes known as "creeping" because the biofilm appears to creep in the direction of the flow.

Quorum sensing is a vital attribute to the microbial network. It is the mechanism that allows the biofilm to form an effective community. Quorum sensing allows the network to collectively know when it is safe to branch out and form towers, or when the biofilm has reached a sustainable-enough population to transcend into the dispersion stage. If the phases of biofilm development simply progressed with time, the dispersal and branching stages may onset at a point that compromises the entire network—quorum sensing allows for a variable growth that accommodates both quick and slow growth processes.

2.1.3 Biofilms in the Industry

The facility for biofilm formation may pose problems in manufactured goods that are ideally kept sterile. Biofilms are a prominent obstacle in both medical and industrial fields. They are normally responsible for infection, persistent infection, and contamination in medical contexts. Some medical complications consequent of biofilm nuisance are: cavities, gingivitis, and periodontitis (all

Figure 2-5 – Methods of biofilm distribution [3].

caused by dental plaque), persistent infection from diseases such as cystic fibrosis pneumonia, otitus media (ear infection), various tract infections, some ulcers, tonsillitis, and osteomyelitis (bone disease) among others, contamination, drain blockage, and endocarditis from various types of catheters, and infection as a result of contamination of implemented bodily devices such as prosthetic implants, contact lenses, pacemakers, and artificial tubes [3].

Figure 2-6 – Chemical biofouling of a pipe in a factory [3]

Corrosion or complication ensuing from biofilms in the industry is termed *biofouling*, usually used when a device has become dominated by a biofilm, reducing its efficiency or utility altogether. Some standard examples of biofouling are: cosmetic degradation of toilet bowls, reduced heat and mass transfer in cooling water towers, reduced heat transfer in heat exchangers, degradation of product quality in paper manufacturing, contamination in food processing, flawed prints or machine failure in photo processing, health risks and cosmetic degradation in pools, clogging of pipes and drains, contamination of household surfaces, and biodeterioration in processing equipment and sewage systems [3].

It is for this reason that so much research has been done in an attempt to hinder the development, or eradicate, existing biofilms. Our historical notions of planktonic bacteria induced a setback in our treatment of infection and disease, because over 99% of bacteria in nature are sessile; the ratio of bacteria that exist as a part of a biofilm to planktonic (historically ideal) bacteria is on the order of 1,000-10,000:1. Up until recently, all modern antibiotics were developed in response to the planktonic model of bacteria. In reality, biofilms are about 1,000 times more resistant to antibiotics than their planktonic counterparts for several different reasons [3]. This failure in proper medical advancement can be attributed to the stern influence and wide acceptance of an established convention in science.

2.1.4 Biofilm Resilience

There are several processes that inhibit the effectiveness of antibiotics in biofilms: diffusion/penetration, stress response, antimicrobial neutralization, persister cells, and nutrient utilization. The first obstruction posed by the biofilm is the slowed rate of diffusion of the antibiotic within the organic film. Antibiotics developed to fight planktonic microbes are effective because of the quick rate of diffusion in water, and the need to only penetrate a single cell. However, in a microbial network the rate of diffusion is greatly reduced because diffusion time scales by the square of the distance—diffusion across ten cells will take one hundred times longer than a single cell [11]. It was believed for some time that the antimicrobials were not able to penetrate to the center of the biofilm but studies have shown that this is not true [11]. A familiar instance in which to apply this slowed diffusive rate could be shown in using mouthwash to treat dental plaque. Cunningham et al. have shown that in order for mouthwash to effectively penetrate the dental plaque in your mouth, you would have to rinse for around 450 seconds.

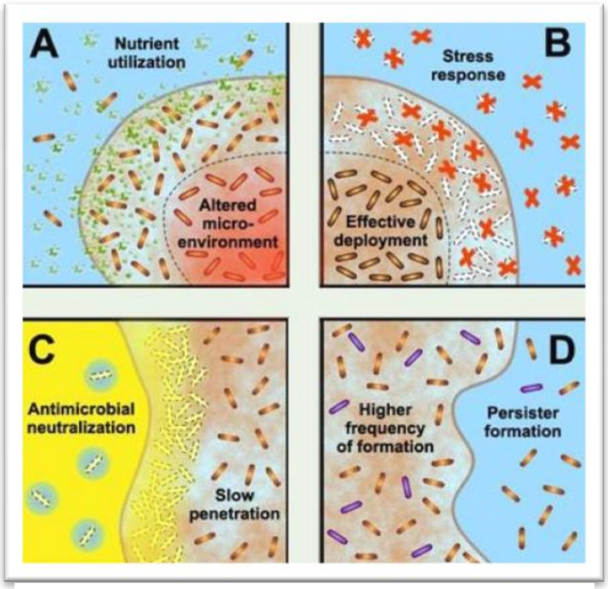

Figure 2-7 – Biofilm defense strategies. These mechanisms are part of the reason why biofilms are so hard to kill.

A second obstacle the antibiotics must overcome is the natural stress response of the target microbe. Conventional antibiotics are able to kill a planktonic cell before it has a chance to initiate its stress response—similar to the human immune system that can acquire a resistance to a certain strain of threat. When an antimicrobial agent penetrates a biofilm, the innermost cells have more time to activate their stress response and adapt to the malignant stimulus, perhaps via some other form of intracellular communication. In effect, using an ineffective antibiotic on a biofilm actually makes it stronger!

In a somewhat similar defense as stress response, the constituents of the biofilm have the ability to produce persister cells. These persister cells are immune to all bactericides and are known as multi-drug tolerant (MDT)—effectively making them impossible to kill chemically [7]. Persister cells are believed to be largely responsible for the survival of biofilms, and thus in themselves become the focus of many researchers [12]. These MDT cells may be seen as a stress response adaptation of the biofilm. Since the persister cells cannot be killed conventionally, they ultimately ensure the survival of the colony.

2.1.5 Biofilm Treatment

It may seem as though it is impossible to combat biofilms given the variety of defense mechanisms they demonstrate, but there seem to be a few treatments that are somewhat effective. The two primary treatments of biofilms used in the field are chlorine and quaternary ammonium compound (QAC). Chlorine attacks the structure of the biofilm itself and works by attempting to remove the film while QAC attempts to kill the constituent cells in the ECM.

While there are methods that attempt to treat a surface already inhabited by a biofilm, there currently is no 100% successful method of preventing biofilm growth. There have been many potential solutions to this, but none of them truly solve the problem.

As bad as biofilms may seem, people have found ways to use them to our advantage. One major example of how we have manipulated biofilms is in water treatment. Water is passed through filters covered in biofilm—cleansing the water of any microbial contaminant it may have had in it. This may sound counterproductive but the organisms in the water are incident to the EPS formed by the biofilm on the filter, and become stuck in the substance as well.

Not all naturally-occurring biofilms are harmful either, biofilms in the environment for the most part help to stabilize the health of the ecosystem they are in. Biofilms are extremely good at adapting to new stimulus, and thus biofilms in soil and water contribute to the homeostasis in their ecosystem when a foreign contaminant is introduced. For example, biofilms assist in the recovery of an oil spill on land or in water. Biofilms in soil metabolize harmful chemicals that might end up in local watersheds through *bioremediation*.

One plan of attack on biofilms is to attempt to form a better understanding of how they form and interact with their environments. There are several different aspects of biofilm formation that could potentially be studied; perhaps the most basic, bacterial adhesion. If bacterial adhesion could be prevented biofilms would be unable to form. It is for this reason that bacterial adhesion is among the most researched field of biofilm prevention. An understanding of the forces involved during bacterial attachment would provide a solid foundation from which to begin the prevention of adhesion.

2.2 Bacterial Adhesion and Force Modeling

2.2.1 DLVO Theory- A Brief History

In 1941, a profound theory explaining the stability of lyophobic colloids (later applied to bacterial adhesion) was formulated by Boris Derjaguin, Lev Davidovich Landau, Evert Johannes Willem Verwey, and Theo Overbeek and was known as DLVO theory [13]. The term lyophobic refers to the affinity of the colloids with the solution they are in—phobic meaning they have no affinity and are therefore easily precipitated.

DLVO theory was first applied to bacterial adhesion in 1971 in an attempt to explain the effects of ionic strength on the reversible stage of adhesion [14]. Since then DLVO theory has been used as a foundation for interactions between microbes and surfaces in gas and liquid media, although experimental data has been found to conflict with DLVO theory especially at relatively close separation distance [13-15]. For this reason, many extensions of the theory have been tacked on to accommodate new experimental data. Some of these new theories include are cell surface hydrophobicity (CSH), thermodynamic approach (entropy and free energy), polymer bridging, Lifschitz theory, electrostatic forces, bulk media approximations (mean-field theory), Helfrich forces, Hofmeister series, and specific ion effects.

Use of only the most credible theories in an extension of DLVO theory results in at least eight new and for the most part ambiguous fitting parameters [13] which is absurd. B.W. Ninham believes that DLVO theory simply cannot be used in biological contexts, and that the original authors of the theory even acknowledged this fact. Derjaguin taught his students that the theory only worked in a certain range of salt concentration, approximately between 0.001 and .05 M, which is more dilute than most biological systems [13].

2.2.2 Classical DLVO Theory

DLVO Theory essentially examines the balance of electrostatic and van der Waals forces in colloid stability. Van der Waals potentials (U_A) are generally attractive while the electrostatic potential energies (U_R) are typically repulsive.

$$U_{total} = U_R + U_A. \tag{2.1}$$

The electrostatic force is a consequence of the electrical double layer, which is associated with a planar surface and a spherical particle [4]. This force is typically repulsive in biological systems because both surfaces and microbes in aqueous solutions are negatively charged. [4] Microbial Adhesion to Surfaces (1980) describes the source of the electrical double layer quite nicely. The abridged explanation is that the charged surface will attract counter ions from the surrounding solution, resulting in a higher concentration of the counter ions at the boundary of the surface than the rest of the bulk media. This concentration forms a theoretical layer known as the Gouy-Chapman diffuse electric double layer. The particle will form a double layer of its own and the electrostatic force is felt when the two diffuse layers overlap.

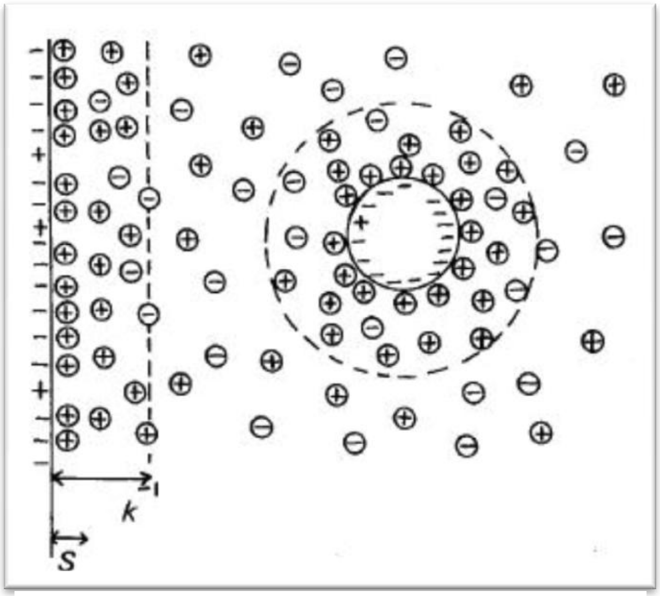

Figure 2-8 – The electrical double layer of a spherical particle and planar surface [4].

$$U_R = \pi \varepsilon_r \varepsilon_o R\left[2\,\psi_1\psi_2 \ln\left(\frac{1+e^{-\kappa D}}{1-e^{-\kappa D}}\right) + \left(\psi_1^2+\psi_2^2\right)\ln\left(1-e^{-2\,\kappa D}\right)\right] . \qquad (2.2)$$

Here the ψ represent surface potentials, r is the radius the microbe, the epsilon are relative and free-space permittivity, κ is the inverse Debye length, and D is the separation between surfaces.

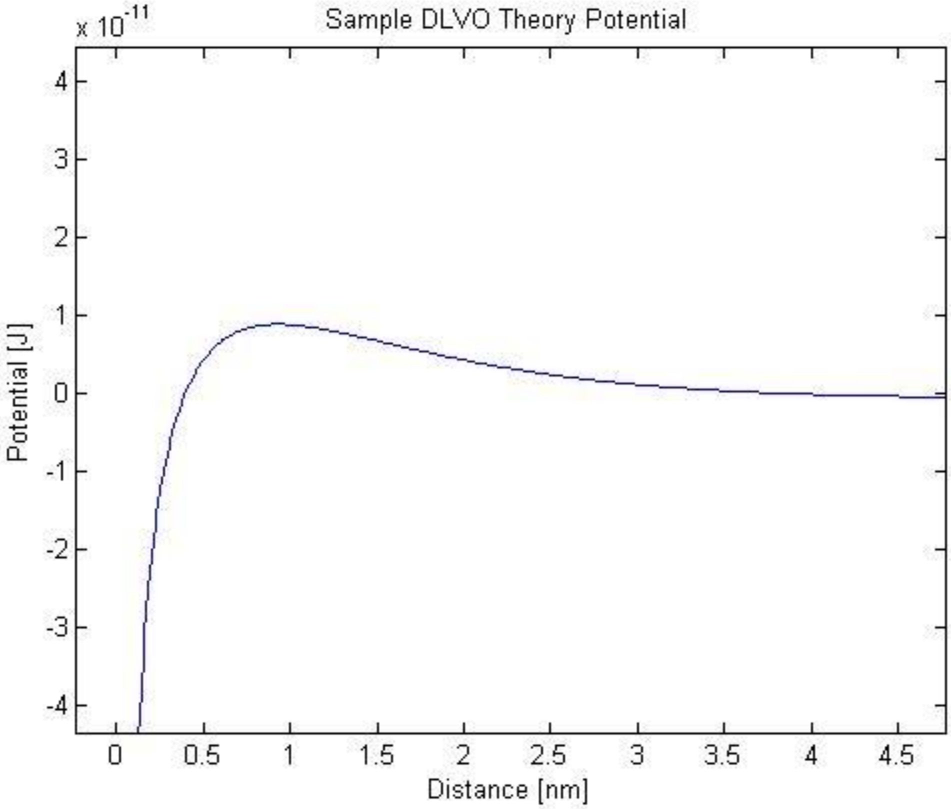

Figure 2-9 – A plot of the DLVO potential using arbitrary characteristic parameters.

Van der Waals forces are a consequence of fluctuations in the polarization of individual molecules or atoms and can be either attractive or repulsive. The fluctuations in polarization are a result the electrons moving relative to the nucleus of the atom; positions close to atoms or molecules will experience fluctuations in electric potential due to this motion.

$$U_A = -\frac{Ar}{6\,\mathrm{D}}. \tag{2.3}$$

The *A* is the Hamaker constant and r is the radius of the bacteria.

Perhaps counter-intuitively, the van der Waals forces are long-ranged in comparison to the electrostatic force with van der Waals potentials acting over distances of about 50-100 nm whereas the electrostatic potential acts at around 0.2-20 nm [3, 14]. This means the particle is (typically) attracted to the surface until it reaches the diffuse layer where it may experience at zero net force sometimes known as the secondary interaction minimum. This occurs at “intermediate” ionic strength and is the reason other extensions of the classical DLVO theory have been adapted in order to explain how bacteria still manages to adhere to a surface. The electrical double layers compress with higher ionic strength so systems with higher ionic strength are more likely to overcome the electrostatic potential while systems with low ionic strength are likely to be repelled [14].

An expression for the DLVO force may be obtained using the relationship between force and potential.

$$\mathrm{F} = -\frac{\partial U}{\partial \mathrm{D}}.$$

$$F = \frac{\varepsilon_r \varepsilon_0 R\kappa}{1-e^{-2\kappa D}}\left[\Psi_1\Psi_2 e^{-\kappa D} - \frac{1}{2}(\Psi_1^2+\Psi_2^2)e^{-2\kappa D}\right] - \frac{AR}{6D^2} \qquad (2.4)$$

where $R = \frac{R_t R_s}{R_t + R_s}$, the reduced tip radius (R_s is the radius of the sample and R_t is the tip radius).

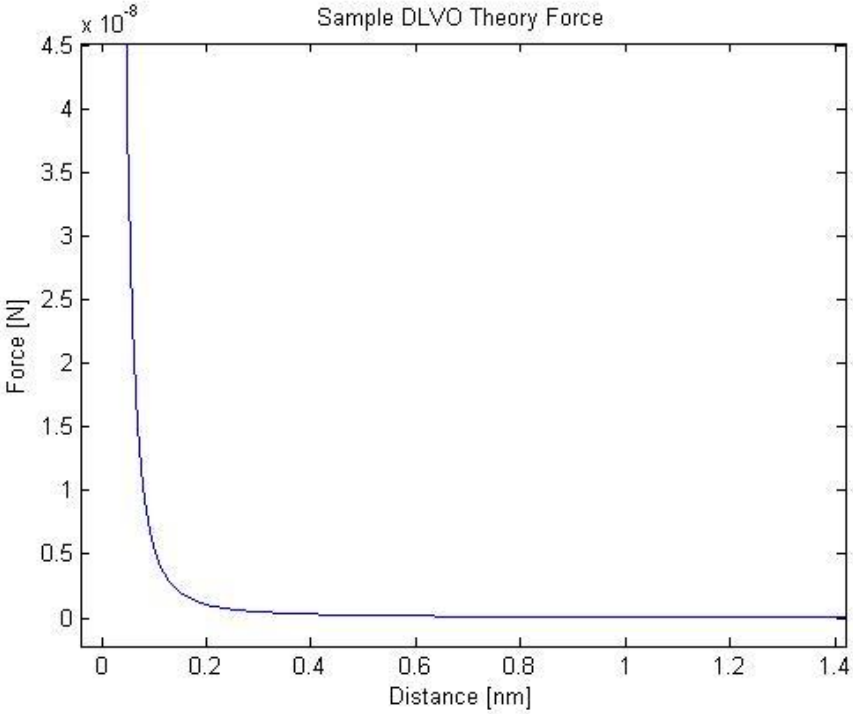

Figure 2-10 – A plot of DLVO force using arbitrary characteristic parameters.

2.2.3 Assumptions of Classical DLVO Theory

One of the most basic assumptions of DLVO theory is that the colloids behave as inert particles (which is certainly not true for bacterial cells) [14]. The surfaces of both the substrate and colloid are also assumed smooth and solid. Other assumptions are as follows: the aqueous solution is uniform up to the interfaces of each surface, the electrostatic and van der Waals forces are independent and additive, the boundary conditions of the electrical double layer are constant potential, the double layer potential is calculated by using a “smeared out” surface charge approximation in conjunction with the non-linear Poisson Boltzmann equation for point charges, the van der Waals forces are computed under the assumption that the aqueous solution is uniform in density and orientation, contact angles are ignored, and repeptisation presented a problem [13].

2.2.4 Why DLVO Theory Isn’t Adequate for Biological Systems

The inadequacy of DLVO theory lies within a couple of its assumptions and limitations. The most significant limitation is the small range of salt concentrations in which the theory has been shown to be accurate, which do not include concentrations found in most biological systems. DLVO theory appears to be a good approximation in systems with low salt concentrations (<0.05 M) where the dominant forces are electrostatic [15]. Ninham et al. argue this to be the primary downfall of DLVO theory in biological systems because of specific ion effects such as dispersion forces. In the four experiments they conducted, they found that DLVO theory typically conflicts with ionic-dispersion data at distances closer than 8 nm and even produced opposite forces at distances between .6-3 nm in biological conditions [15].

This problem arises from the assumptions in the boundary conditions and the smeared out surface charge approximations. The simplified boundary conditions ignore the entropy of the electrical double layers (which is somewhat related to ionic dispersion) and the smeared approximation is only a good approximation at extreme ionic strengths [13]. Essentially the approximations neglecting the discreteness of the ions are no longer valid in biological contexts.

Another assumption worth noting is that the fluid has bulk properties even at the surfaces of the substrate and particle; this implies that their respective interfacial free energies are infinite.

2.2.5 Extensions of DLVO Theory and Proposed Theoretical Forces

Several extensions and “decorations” have been amended to DLVO theory in order explain potentials that DLVO theory does not predict itself. Perhaps the most accredited of these extensions are hydration effects such as cell surface hydrophobicity (CSH), molecular size and the continuum approximation (dealing with molecule oscillations and fluid boundary conditions), Lifschitz theory (using dielectric susceptibility to account for many-body forces), polymer bridging, and steric interactions (due to surface fluctuations).

2.2.6 Surface Forces Apparatus and the First Force Model

Some of the first measurements of interactions between surfaces covered with polymers were conducted on the surface forces apparatus (SFA) by Jacob Israelachvili, S. J. Alexander, and Pierre-Gilles De Gennes [16]. The SFA was the predecessor of the atomic force microscope (AFM) and was able to resolve forces at distances of 1 Å and magnitudes of 10^{-8} N. This device had the more specific intent of measuring forces between two surfaces while the AFM was adapted to measure forces on a much smaller scale. The AFM is a much more widely-used device than the SFA these days but the force models derived by Alexander and de Gennes have been adapted for application with the forces observed by the AFM.

Modern AFM force models are primarily based upon results obtained by de Gennes with the help of Alexander. His original equation determined the force per unit area of two plates with grafted polymer brush surfaces.

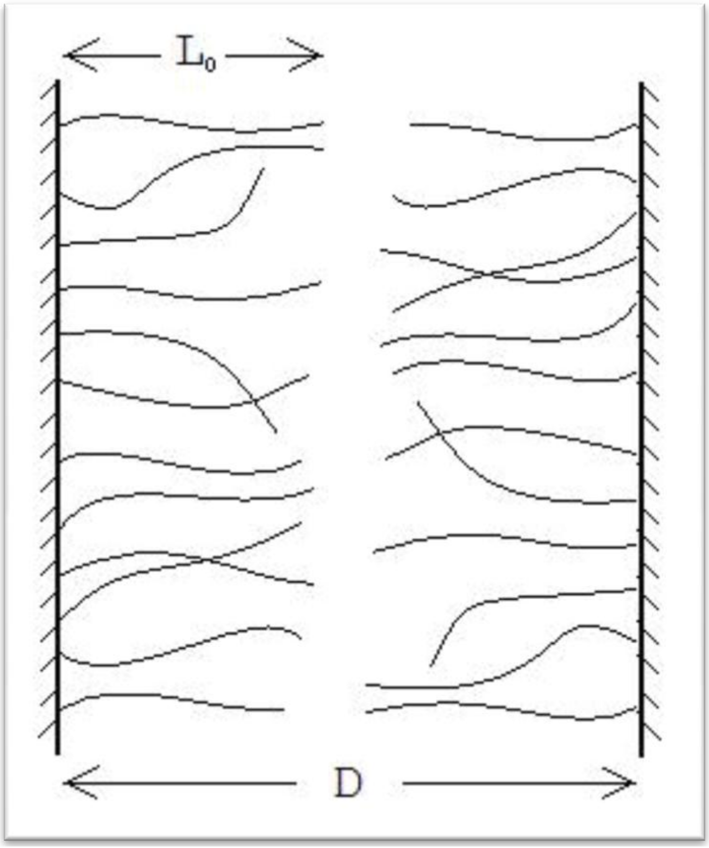

Figure 2-11 – A depiction of experiments conducted with the surface forces apparatus involving two polymer brushes.

$$P \approx \frac{k_B T}{s^3}\left[\left(\frac{2L_0}{D}\right)^{9/4} - \left(\frac{D}{2L_0}\right)^{3/4}\right] . \tag{2.5}$$

This is a pressure, where k_B is the Boltzmann constant, T is the temperature in Kelvin, Γ is the grafting density, D is the separation distance, and L_0 is the equilibrium thickness of the brush. The dominant term is related to the osmotic pressure of the polymer brush and the receding term is a result of the elasticity of the polymers [16].

2.3 AFM Force Models

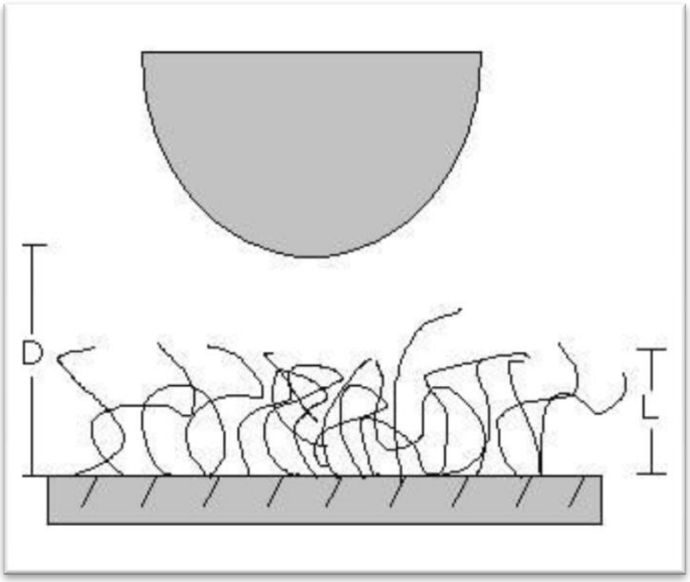

Figure 2-12 – Parameters D and L in the approach of an AFM tip.

This model applies to a two-surface interaction where both surfaces are coated with polymers. In order to adapt the formula to AFMs a sphere-flat geometry interaction must be derived. After some effort, the following model is obtained (for a complete derivation see Appendix A).

$$F_{sphere} = \frac{8\pi k_B TRL}{35s^3}\left[7\left(\frac{L}{d+h}\right)^{5/4} + 5\left(\frac{d+h}{L}\right)^{7/4} - 12\right] \tag{2.6}$$

The result of this derivation differs from most references [17-19] but the discrepancy primarily lies within the leading coefficient. Instead of using a grafting density the parameter *s* has been introduced. The interpretation of this parameter also has some controversy; it has been called the spacing between polymers on the surface as well as the distance between cross links in the brush. The *h* in this equation is an offset representing the point of incompressibility of the polymer brush as illustrated in Figure 2-13.

Alternative models were also derived for pyramidal and conical tip geometries. The derivation of these models may be found in Appendix A. θ is the half-angle of the tip.

$$F_{pyramid} = \frac{128k_B TL^2}{385s^3}\tan^2\theta\left[77\left(\frac{L}{d+h}\right)^{1/4} + 33\frac{d+h}{L} - 5\left(\frac{d+h}{L}\right)^{11/4} - 105\right]. \tag{2.7}$$

$$F_{cone} = \frac{32\pi k_B T L^2}{385 s^3} \tan^2\theta \left[77 \left(\frac{L}{d+h}\right)^{1/4} + 33\frac{d+h}{L} - 5\left(\frac{d+h}{L}\right)^{11/4} - 105 \right]. \qquad (2.8)$$

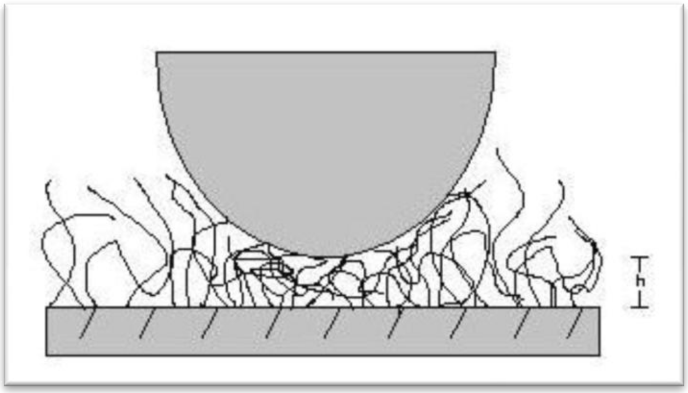

Figure 2-13 – The point *h* where the bacterial brush becomes incompressible.

Another factor that must be taken into consideration when converting to the AFM model is the two that precedes the equilibrium thickness of the polymer brush. This two is meant to account for the double-surface system where both surfaces are covered in polymers.

$$F_{sphere} = \frac{16\pi k_B T R L}{35 s^3} \left[7\left(\frac{2L}{d+2h}\right)^{5/4} + 5\left(\frac{d+2h}{2L}\right)^{7/4} - 12 \right]. \qquad (2.8)[18]$$

This model represents a situation where the AFM tip is also covered in polymers.

For the regime where the AFM tip is in contact with the polymer brush, the force expression may be approximated by an exponential.

$$F_{brush} \approx 50\, k_B T R L \Gamma^{\frac{3}{2}} e^{-\frac{2\pi D}{L}}. \qquad (2.9)[19]$$

This approximation is valid only when the tip is within the brush and above the maximum indentation depth of the layer, roughly for D/L_0 ratios between 0.2 and 0.9 [17, 19]. Here again is an example of the discrepancy in the leading coefficient.

Most of the formulas shown thus far share a similar, classical derivation. Other derivations have been performed using methods such as mean-field theory and thermodynamics. These models can get very complicated and may involve relatively abstract terms like surface potential and permittivity. Here is an equation derived using DLVO theory as an example:

$$F = \frac{a_t a_b}{a_t + a_b}\left[2\pi\varepsilon_r \kappa e^{-\kappa D}\left(\frac{\psi_t^{2} e^{-\kappa D} + \psi_b^{2} e^{-\kappa D} - 2\psi_t\psi_b}{e^{-2\kappa D} - 1}\right) - \frac{A}{6D^2}\right] . \qquad (2.10)[20]$$

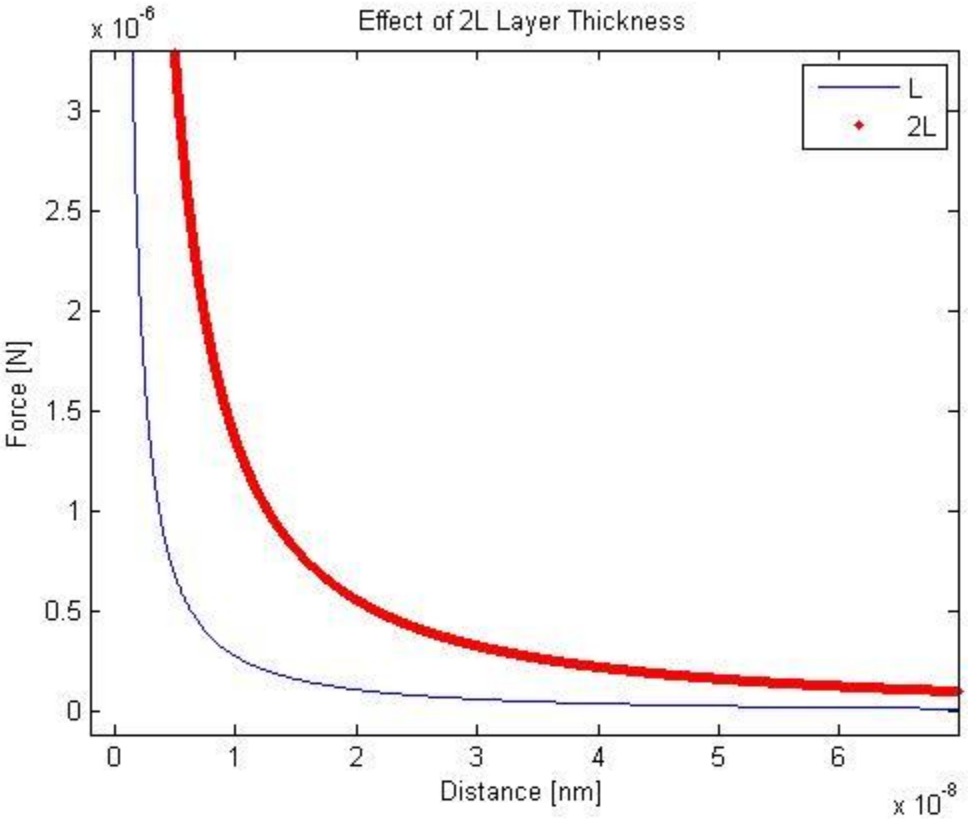

Figure 2-14 – The difference in theoretical approach when *L* or *2L* is used. The proper equation has a much shorter non-zero interaction, which is to be expected.

This expression contains many derived constants like the relative permittivity (ε_r), the surface potentials of the bacteria and tip (ψ), and the Hamaker constant *A*. The *a's* represent the respective radii of the tip and bacteria. κ is the inverse Debye length defined as:

$$\kappa = \sqrt{\frac{2e^2 N_A I}{\varepsilon_r \varepsilon_0 k_B T}}\,. \tag{2.11}$$

Where N_A is Agravados number (6.022×10^{23}) and *I* is the ionic strength of the solution.

2.4 Polymers, Adhesion, and Hysteresis

2.4.1 Polymer Physics

The word polymer is Greek in origin—*poly* meaning "many" and *mer* meaning "part." The parts of a polymer are known as monomers or *primary molecules* which are repeated thru out the polymer chain. Although polymer lengths vary quite wildly, the symbol *Z* is used to denote the number of monomers or the *degree of polymerization* of a polymer [21].

If ℓ denotes the length of a monomer, *n* is the length of a bond, and *Z* is the degree of polymerization, the total length of a polymer is then,

$$L = \ell Z. \tag{2.12}$$

The *L* here is not the same as the *L* used in force modeling equations, but the stretched out length of a single polymer. In reality, polymers are rarely (if ever) completely straight, but this formula could be applied to situations where the polymer experiences a force that causes it to stretch which will be investigated shortly. Polymers are capable of bending at the sites where monomers bond together. The classification of the bond dictates the degree of freedom which the new unit is free to bend in.

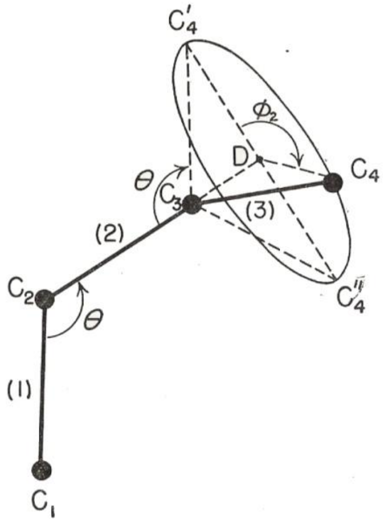

Figure 2-15 – A polymer of third degree with four binding sites, showing possible bond orientation angles [22].

Although the total length of a polymer can be of use, its displacement is of more common interest. Assuming a primitive model where all angular configurations are equally possible, the average displacement of a polymer is,

$$L_x = \ell Z(Z-2) < cos\theta > \ , \tag{2.13}$$

where $\langle \cos\theta \rangle$ is averaged over all angles. Cosine is zero when averaged over all angles so this expression is not adequate. Using a root mean square method to describe displacement,

$$L_{RMS} = \frac{\ell Z}{\sqrt{3}}. \tag{2.14}$$

A random-walk simulation can be used to demonstrate this principle; using ℓ to denote step length and *Z-1* for the number of steps. Figure 2-16 shows an example polymer described by these conditions.

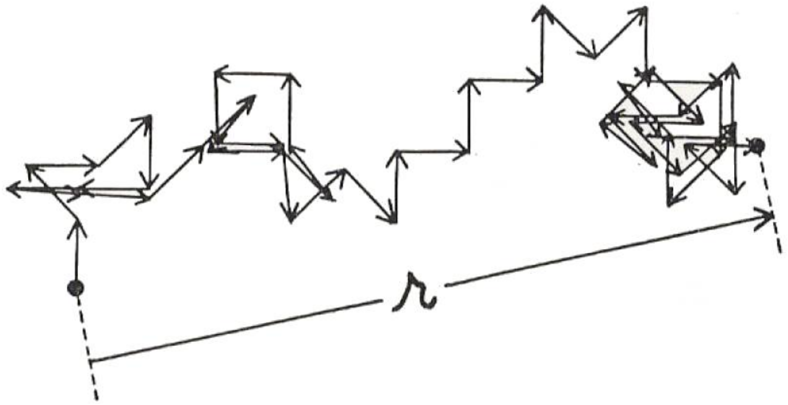

Figure 2-16 – A polymer without angle restrictions. , in this case r is used for displacement instead of L_{RMS} [22].

As was stated earlier, real polymers have constraints on their ability to bend as a result of the type of bond formed. The root mean square displacement of a polymer with bond angle restrictions in three dimensions is given by,

$$L_{RMS} = C\sqrt{Z}\,, \qquad (2.15)$$

where C is a characteristic parameter of the polymer chain structure proportional to ℓ. A more accurate representation of a polymer can now be made using random-walk where the change in direction relative to the last step is restricted by characteristic angles.

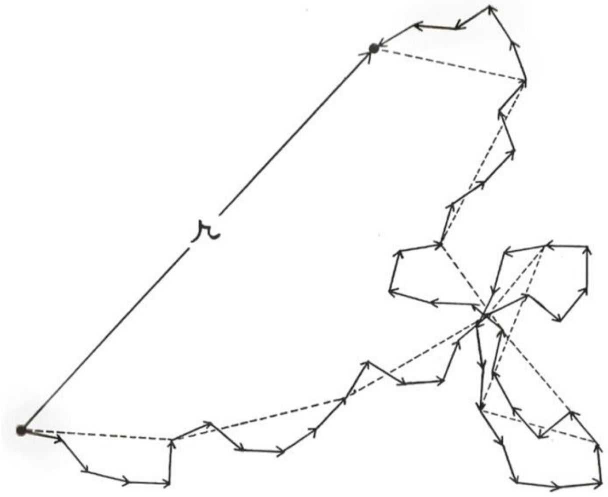

Figure 2-17 – A polymer of 50 monomers with bond angle restrictions of 90°[22].

2.4.2 Polymer Bridging and Hysteresis

Many experiments have detected a hysteresis in the retraction of the AFM cantilever. This hysteresis is a result of polymers attaching to the tip of the cantilever and then snapping off when a certain distance is reached. Figure 2-15 depicts this hysteresis and corresponding events in the tip-brush interaction.

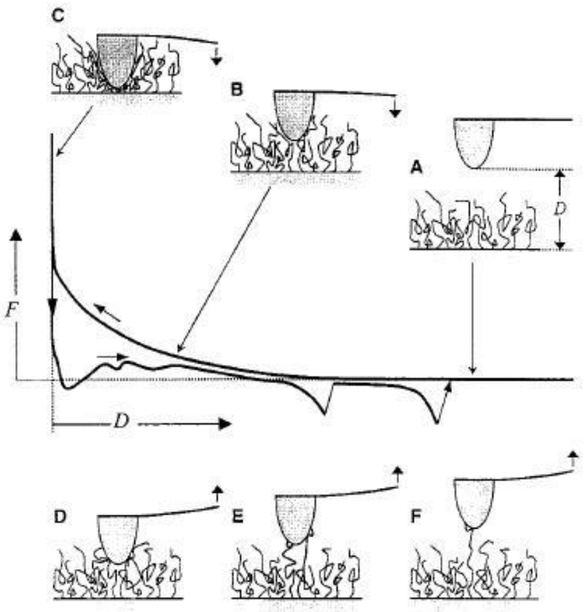

Figure 2-18 – Explanation for the hysteresis observed in a force retraction curve [19].

There are several different models used to describe polymer dynamics. The most simple of these models is the freely jointed chain (FJC)—described as a series of connected monomers that have equal probability of being in any configuration angle seen in Figure 2-16. This model can be thought of as a chain of rods in the statistical mechanics sense. The force required to stretch a polymer by length *D* is given in Equation 2.16.

$$F_{st} = \frac{k_b T}{l} \angle^{-1}\left(\frac{D}{L}\right). \qquad (2.16)\ [17]$$

The $\angle^{-1}$ is the inverse Langevin function, and ℓ is the length of the monomers. Taking the first four terms of this function gives:

$$F_{st} = \frac{k_b T}{l}\left(3\frac{D}{L} + \frac{9}{5}\left(\frac{\mathrm{D}}{L}\right)^3 + \frac{297}{175}\left(\frac{\mathrm{D}}{L}\right)^5 + \frac{1539}{875}\left(\frac{\mathrm{D}}{L}\right)^7\right). \qquad (2.17)\ [17]$$

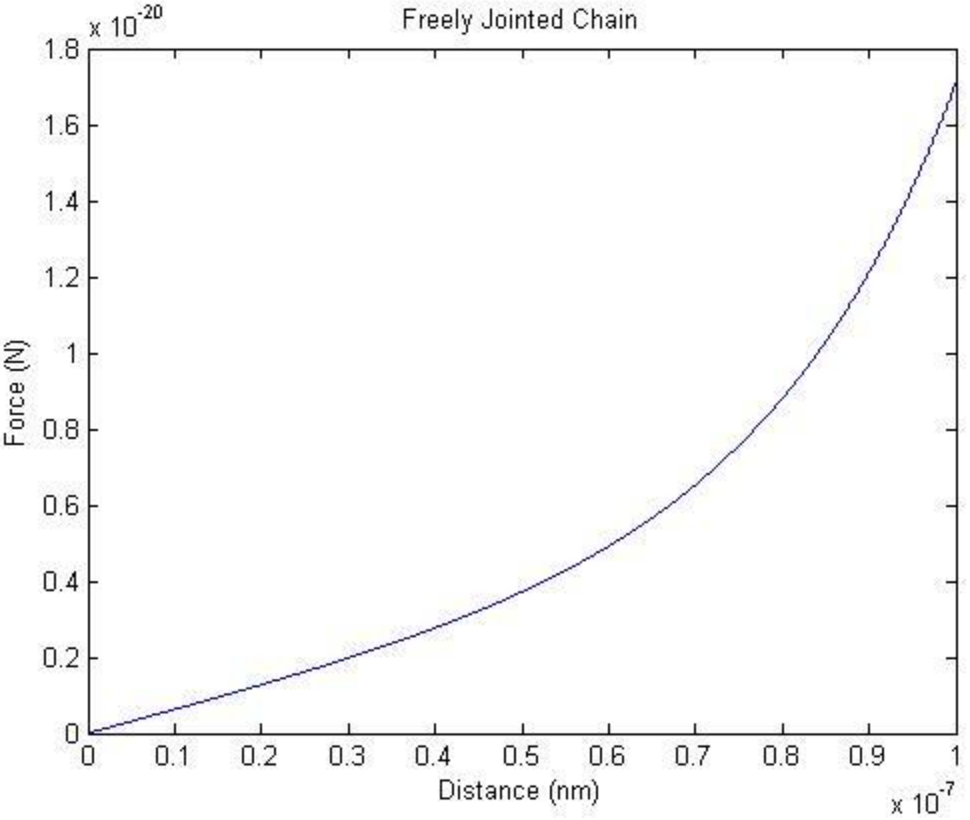

Figure 2-19 – The force required to stretch a freely-jointed chain using arbitrary characteristic parameters.

This is the crudest of polymer chain models; the freely rotating chain (FRC, Figure 2-17) and hindered rotation model (HRM) make logical improvements upon the FJC. The FRC incorporates angles limited by chemical bonds in the polymer; all torsion angles are still equally likely. The HRM considers the potential energy of configurations—making the probability of each configuration a function of the Boltzmann factor:

$$P(\theta) \propto e^{\left(-\frac{U(\theta)}{k_B T}\right)}. \qquad (2.18)\ [17]$$

The most complex polymer chain model may be worm-like chain (WLC) model. In this model persistence length (the length of the lowest energy configuration for the polymer) is taken into account; work must be done in order to stretch or compress the polymers from their persistence length. This is because each monomer is considered isotropic or independently flexible and ℓ is no longer representative of all monomers. The WLC has been used to successfully describe the stretching of DNA, polysaccharides, poly(dimethysiloxane) in heptanes, and the protein titin [17].Hans-Jurgen Butt et al. determined the worm-like chain (WLC) model description of polymers best fitted the hysteresis data. The force required to stretch a polymer is:

$$F_{st} = \frac{k_B T}{b}\left[\frac{D}{L} + \frac{1}{4(1-D/L)^2} - \frac{1}{4}\right]. \qquad \text{(2.19) [17]}$$

Here b is the persistence length of the polymer. Note that this equation is an approximation over this unbounded range of *D.* For distances such that *D<<L* the equation becomes:

$$F_{st}(\mathrm{D}) = \frac{3\, k_B T D}{2\, bL}, \qquad (2.20)$$

[17]

and for forces greater than $k_B T/b$

$$F_{st}(\mathrm{D}) = \frac{k_B T}{4\, b\left(1-\frac{\mathrm{D}}{L}\right)^2}. \qquad (2.21)$$

[17]

This is an important effect to model in the lab because it will reaffirm the brush-like nature of the alginate substitute.

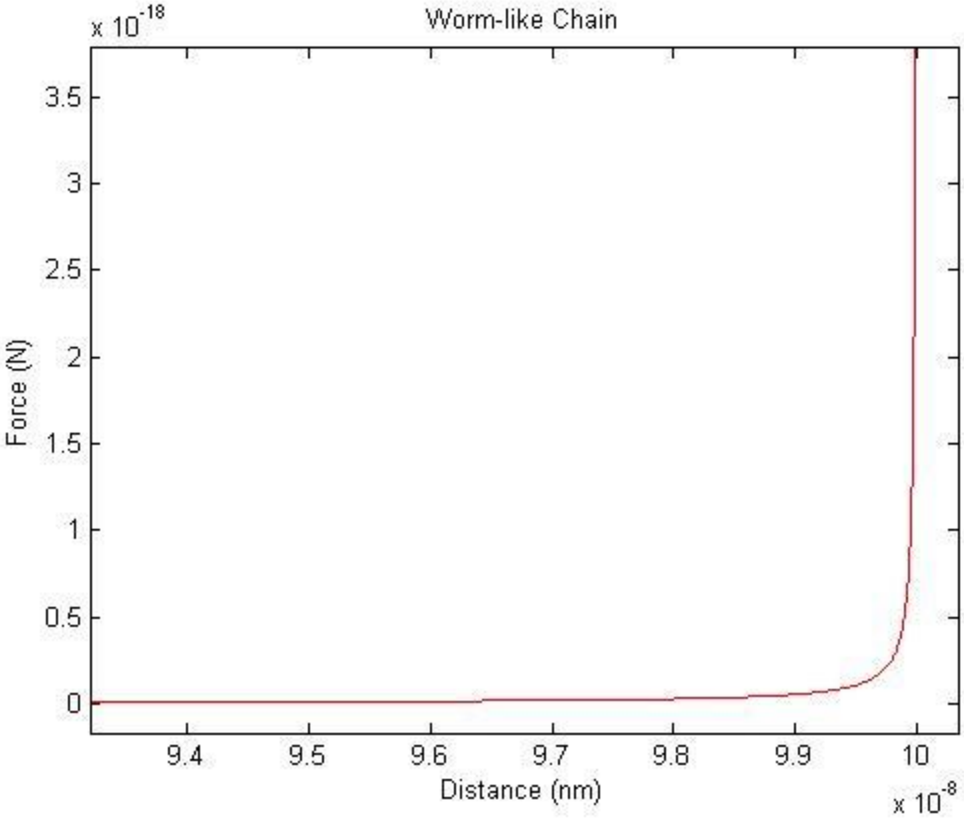

Figure 2-20 – The force required to stretch a worm-like chain using arbitrary characteristic parameters.

2.5 Brush Modeling and Surface Properties

Many complications accompany observations of force when using live bacterial cells, the biggest of these being the conformability of the cell itself. It is difficult to decouple the interactions between the AFM tip and the polymer brush from the tip and cell surface because the cell is so malleable. Some potential solutions to this problem are to rigorously decouple the interactions, use a chemical to harden the surface of the bacteria, or simply attempt to replicate the polymer brush with different conditions. For sake of simplicity decoupling was not attempted. Using a chemical to harden the bacteria may also have unforeseen effects on the polymer brush or overall force modeling so this method was also avoided.

2.5.1 Alginate

In an attempt to replicate the surface of a bacterial cell, sodium alginate, a polymeric molecule with high molecular weight that is derived from seaweed was used. Alginate is actually found in the EPS of certain biofilms such as *pseudomonas aeruginosa*—the cause of cystic fibrosis in the lungs [23]. Its empirical formula is $NaC_6H_7O_6$. The alginate will be bound to glass slides using EDC/NHS (1-ethyl-3-[3-dimethylaminopropyl]carbodiimide/ N-hydroxysuccinimide) binding [24] and with any luck will recreate the bacterial surface environment without the complication of coupling.

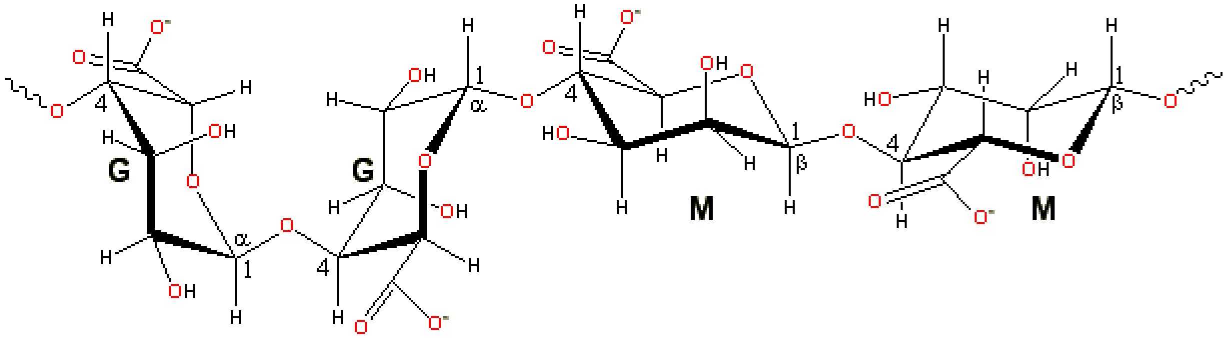

Figure 2-21 – Molecular structure of alginate. [25]

Alginate is made up of alternating residues, β-(1⟶4)-linked D-mannuronic acid (M) and α-(1⟶4)-linked L-guluronic acid (G). Possible configurations are MMMMMM, GGGGGG, or GMGMGM [25].

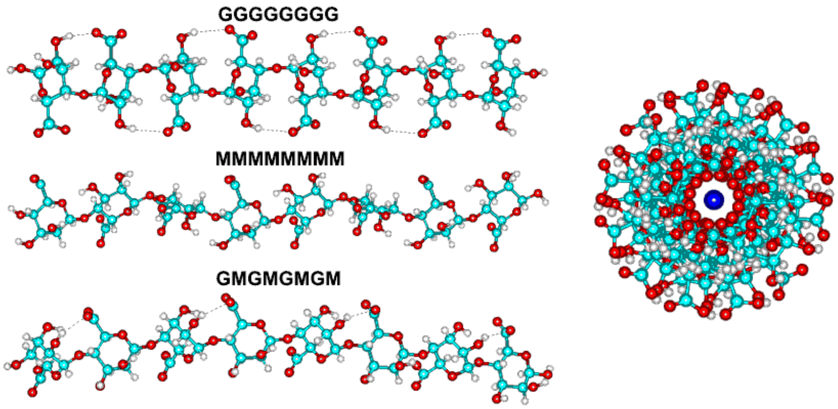

Figure 2-22 – Physical structure of the residue sequences and an axial view of a possible configuration of the polymer [25].

Figure 2-22 shows physical configurations of the alternating residues as well as a cross-sectional view down the polymer chain. A potential problem arises here: it appears as though the chemical make-up of the end of the chains is similar to the radial shell. This could mean that the polymer is equally likely to bind with the EDC on its ends as its midsection. In this case a condition similar to the one illustrated in Figure 2-23 would be observed.

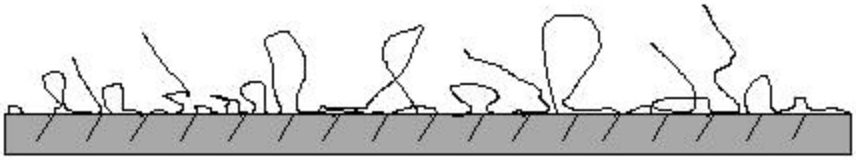

Figure 2-23 – A scenario where the alginate binds indiscriminately to the glass slide.

If the above circumstance actually occurred it may not be of great importance, because it appears similar to a dilute solution of ideal polymers. However, in the worst-case-scenario the alginate would be completely bound to the slide laying flat. In that case, alginate would fail to model a brush or anything similar to what the equations examined in Section 3 attempt to describe.

2.5.2 Surface Properties

As stated earlier, thermodynamic properties of the surface have implications for force modeling. These properties may also suggest the successful binding or presence of the alginate on the glass slide, as well as the uniformity of the surface. For these reasons the parameters such as surface free energy (SFE) and interfacial free energy (IFE) are of interest. The SFE and IFE are components of the Gibbs free energy (energy available to do useful work) and are functions of temperature, pressure, and the number of particles in the system. The Gibbs free energy relating to bacterial adhesion is:

$$\Delta G_{adh} = \gamma_{BS} - \gamma_{BW} - \gamma_{SW}. \qquad (2.22)$$

Here, γ represents the total surface tension—a parameter that can be determined from contact angle measurements. The subscripts *BS, BW,* and *SW* correspond to bacterial-surface, bacterial-water, and surface-water interactions.

$$\begin{bmatrix} \gamma_i^{LW} \\ \gamma_i^{+} \\ \gamma_i^{-} \end{bmatrix} = \left\{ \left[\left[2 \cdot \begin{bmatrix} \sqrt{\gamma_W^{LW}} & \sqrt{\gamma_W^{-}} & \sqrt{\gamma_W^{+}} \\ \sqrt{\gamma_D^{LW}} & \sqrt{\gamma_D^{-}} & \sqrt{\gamma_D^{+}} \\ \sqrt{\gamma_F^{LW}} & \sqrt{\gamma_F^{-}} & \sqrt{\gamma_F^{+}} \end{bmatrix}^{\cdot} \cdot \begin{pmatrix} \gamma_W \cdot \left[\cos(\theta_W) + 1 \right] \\ \gamma_D \cdot \left[\cos(\theta_D) + 1 \right] \\ \gamma_F \cdot \left[\cos(\theta_F) + 1 \right] \end{pmatrix} \right] \right] \right\}^2 \tag{2.23}$$

Equation 2.23 shows how the surface tensions are calculated from the contact angle measurements using water, diiodomethane, and formamide. LW stands for Lifsthitz-van der Waals, + denotes electron-donor, and -, electron-acceptor.

2.5.3 The Effect of pH on Polymers

Debby Chang et al. [18] performed a study investigating the interaction between the AFM tip and a polymer brush. They attempted to model both relaxed and compact conditions of the polymer brush. To do this, they varied the pH of the buffer solution that they used. An increase in pH results in a relaxation of the brush, and the individual polymers stretch out and become less tangled. Conversely, a decrease in pH causes the brush to crumple up and form a dense layer.

This is effect provides the foundation for the experiment to be conducted, determining the meaning of the variable *s*, the root or mesh spacing in the polymer brush. A variety of pH's will be used (5, 6, 6.5, 7) and the respective force curves will be modeled by Equation 2.6. If *s* is the root spacing, it will be invariant under change in pH while it would decrease if it was mesh spacing. The mesh spacing hypothesis proclaims that *s* is the distance between polymer cross-links.

3 Experimental

This chapter provides a detailed explanation of the methodology of the experiment.

3.1 The Experiment

3.1.1 Experimental Overview

In each trial, the polymer brush conformation will be manipulated by varying the pH of the buffer solution. This should consequently change the parameters *L, s,* and *h* with each buffer. Several force measurements will be taken in the presence of each buffer to obtain curves of different brush conformations. These curves are then each zeroed in Matlab, and processed in Excel to normalize the force and separation offsets, as well as the calibration error (this compensates for the error involved in drawing the slope during force curve acquisition). Excel also converts from raw AFM data (scanner position and cantilever deflection) to relevant parameters (force and separation). The force curves for each pH will then be averaged to minimize the experimental noise observed in individual force curves. This is done simply in Excel by summing the forces and separations for each curve and dividing by the number of curves summed. A potential caveat of this method is the effect of thermal drift which could potentially mean that force curves are not taken at the same point throughout force curve acquisition for a single pH condition (although the acquisition process may take as little as 30 seconds). The now-averaged force data is fitted in a fitting program such as Matlab, Table Curve, or Excel. All three fitting programs were used in this experiment, and the results may be found in the Results and Discussion section of this report. The curves are fit in a linear plot so that deviation is minimized. The models are then manipulated in such a way that each parameter produces a distinct effect in a semi-log plot, and a curve from each pH buffer is displayed on the same plot in order to visualize the effects of pH on polymer conformation. The details of these procedures are explained later in this chapter.

3.1.2 Trial Conditions

Five separate trials of this experiment were performed. The first three attempted to find a good concentration of alginate to take force curves on. This concentration was found in trial three, and the last two trials attempted to replicate this data. The differences between trials are illustrated below.

Table 3-1 – Trial Conditions

Trial	**1**	**2**	**3**	**4**	**5**
Alginate Concentration (M)	10^{-6}	10^{-9}	10^{-6}	10^{-6}	10^{-6}
pH Succession	5, 7, 9, 7	5, 5.5, 6, 7	5, 5.5, 6, 7	5, 6, 7	5, 5.5, 6, 7

All force measurements and images were taken using a Veeco Dimension 3100 atomic force microscope with the Nanoscope IIIa controller in the presence of a buffer solution unless otherwise stated. The cantilevers used were Veeco Dimension series DNP-S probes with a manufacturer-specified spring constant of 0.12 N/m and a maximum tip radius of 40 nm. These parameters can be determined experimentally for more qualitative results. Figure 3-1 is a scanning electron microscope image of the AFM tip used.

Figure 3-1 – A scanning electron microscope image of the Veeco DNP-S pyramidal AFM tip. The distance from base to tip is about 3.0 µm and the nominal tip radius is 10 nm. Note: colors are inverted [26].

3.2 AFM Background

Perhaps the newest type of microscope, the atomic force microscope (AFM), was invented in 1986 as a successor to the scanning tunneling microscope [27]. These microscopes are capable of achieving atomic resolution (on the order of angstroms or 10^{-10} meters) and can image live samples in solution. The basic principle of an AFM is that it "feels" the surface of a substrate with an incredibly fine tip and records how the tip moves in reaction to the surface. This is achieved by placing this tip on a lever arm called a *cantilever* which is mounted on a scanner. A laser is then focused on the tip of the cantilever and reflected into the center of a photodiode with four quadrants. When the cantilever moves across a surface, it is deflected by surface features and the laser consequently shifts in response on the photodiode. The photodiode converts the reflected laser signal into a voltage depending on how close the reflection is to the center, and in which quadrant the signal is coming from. This voltage can then be converted into units of length, typically nanometers. In order to image regions microns in size, a precise mechanism was needed to move the cantilever in lateral directions. Piezoelectric material—a material that changes shape depending on the voltage that is applied across it—was used to achieve this precision. The reason why this piezoelectric material changes shape with voltage is because its constituent dipoles are arranged randomly amongst the material, when a voltage is applied across the length of this material, the dipoles (on average) align according to the voltage—effectively elongating or shortening the material.

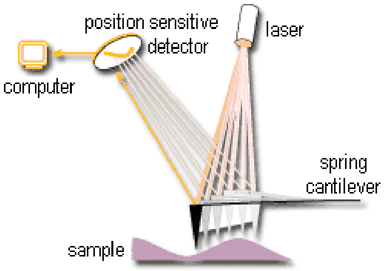

Figure 3-2 – A diagram of how an AFM works [28].

The most relevant function of the AFM to biofilms/polymer research is not its ability to image, but to record force interactions with samples. Just as deflection can be measured to map the surface of a sample it can be used to measure the forces acting on the cantilever at a particular point on the substrate—all that is needed to convert from deflection to force is the spring constant of the cantilever which can also be measured using certain procedures. This was an incredibly important revelation in the field of biofilm and polymer research because it allowed for the direct comparison between theoretical force models and empirical data.

3.3 Sample Preparation

The following sections describe the basic methods used to bind alginate to a glass slide. The detailed step-by-step procedures can be found in Appendix B.

3.3.1 Making the Buffer Solution

The buffer solution is the liquid used to vary pH or ionic strength throughout the experiment. Potassium phosphate mono-basic provided by SIGMA^{TM} was used. This compound (KH_2PO_4) has a molecular weight of 136.1 Daltons. The solution was brought to 0.01 molarity in order to model physiological conditions. The solution was then baked in an Autoclave for an hour. When the solution comes out it is around pH 5. For the purposes of this experiment, separate solutions were brought to pH 7 and pH 9 using pure NaOH. The buffer is to be added to the slide prior to force measurements.

3.3.2 Preparing Alginate Solution

Alginate is the molecule of interest in this experiment. A study on the processes of imaging alginate with an AFM is documented in [29]. The average molecular weight of alginate is 230±60 kDa. In order to achieve a concentration of 10^{-6}, 0.23 g of alginate was mixed in one liter of ultra-pure water (230,000 g/mol x 10^{-6} mol/L).

3.3.3 EDC/NHS Binding

The 1-ethyl-3-[3-dimethylaminopropyl]carbodiimide/ N-hydroxysuccinimide (EDC/NHS) binding method is what binds the alginate to the glass slide. Instructions on the procedure supplied by the chemical provider, Pierce, can be found in [24]. The EDC and NHS solutions are mixed with the alginate stock solution and then bound to the slide with 3-Aminoporpyltrimethoxysilane (aminosilane). The EDC solution is prepared by mixing 0.192g of EDC in 10 mL of ultra-clean water. The NHS solution is also mixed in 10 mL of ultra-clean water but 0.087g is used instead. The EDC should be at a pH of about 7, and needs to be brought down to pH 5.5. This can be done using sulfuric acid. The NHS should be around pH 3 and needs to be brought up to pH 7 which can be done by quickly dipping pure NaOH in the solution. Both solutions are then left in a refrigerated centrifuge (typically overnight).

The EDC/NHS binding method is used to bind carboxylates (-COOH) with amino groups ($-NH_2$). In this case alginate is the carboxylate and aminosilane is the amino group. A more detailed procedure can be found in Appendix B. It is also necessary to clean the glass slides before binding the alginate to them. A procedure for this can also be found in Appendix B.

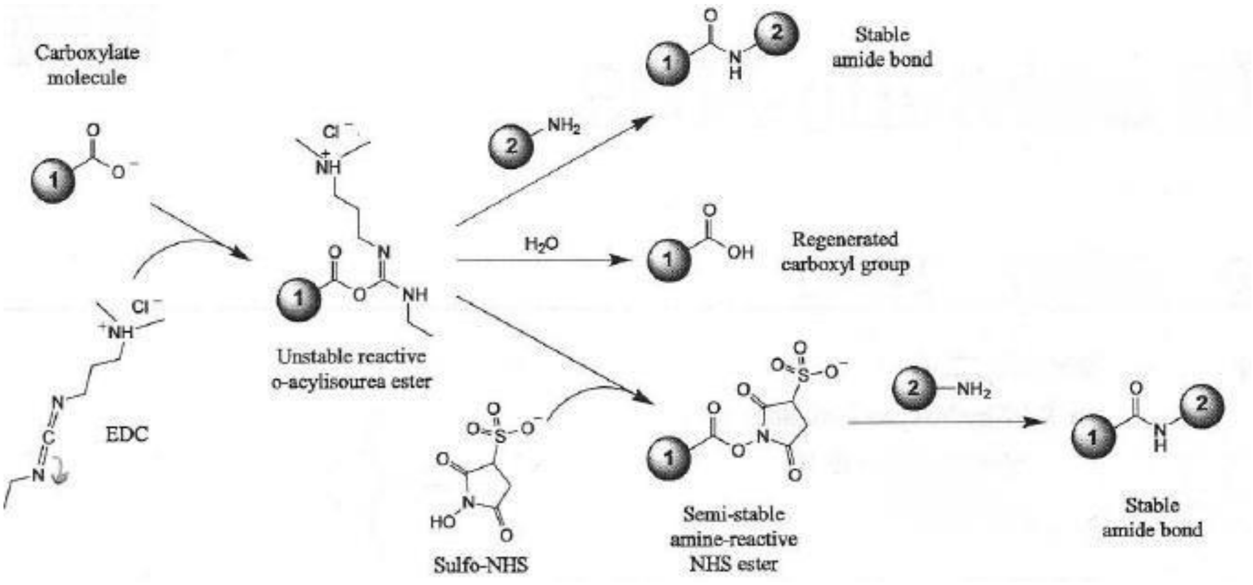

Figure 3-3 – EDC and NHS binding: the EDC binds with Compound 1, and then with NHS. Compound 2 then binds to the NHS via a previously-bound amino group [24].

3.3.4 Contact Angles

The purpose of contact angles are to measure surface free energy (SFE) interfacial free energy (IFE) and hydrophobicity/hydrophilicity. The primary concern with this is to make sure there is alginate on the slide and the bulk characteristics of the alginate layer are not altered after force measurements are taken. Contact angles also provide an idea of how uniform the surface of the substrate is.

Contact angles were taken using a goniometer and the program, DROPImage Standard. It is not necessary that a goniometer be used for contact angle measurements, but it does make it less laborious. An alternative would be to photograph and physically measure the angles of contact between the liquid and the substrate. DROPImage Standard simply measures the angles of contact automatically and averages them to produce a more replicable measurement. Figure 3-4 demonstrates how contact angles are measured.

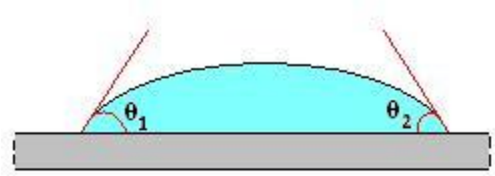

Figure 3-4 – The angles measured in contact angle measurements. The angle that should be used is the average of the two measured angles.

Although contact angles themselves may hint to the presence of something on the substrate, it is more appropriate to calculate surface and interfacial free energy using the observed angles. In order to do so, contact angles must be acquired with diiodomethane, formamide, and water. These values may be used in Equations 2.22 and 2.23 from the Literature Review chapter.

3.4 Force Measurements

The Veeco DNP-S probes are pyramidal silicone-nitride tips and should follow the pyramidal force model according to the manufacturer-specified tip radius. If the radius is actually larger, it is possible that only the spherical portion of the tip enters the alginate brush, and then the spherical force model should be used. Certain procedures may be done to measure the actual tip radius using grafting samples.

A drop of the appropriate pH buffer solution is added to the tip of the cantilever before approach and engagement. The cantilever is now tuned (usually by a program provided by the AFM manufacturer) that emits an ascending audio signal and plots the reaction of the cantilever against frequency. This program attempts to find the resonance frequency of the cantilever so it can be properly oscillated during imaging. The scanner then begins approach to the surface. After the bubble on the tip of the cantilever makes contact with the surface, more buffer solution may be added surrounding the tip. After the tip is engaged, it is important to tune the cantilever once again.

Before and after force measurements, topographical images were taken of the surface in order to observe any adverse effects of the force acquisition process. Force curves were taken at two separate positions on the substrate, and about fifteen curves were saved for each position.

The sample is then removed and the buffer solution is carefully dried from the tip and slide. Special care must be taken in the drying of both—pressure on the cantilever could break the tip and too much pressure on the slide could affect the surface topography or potentially remove the alginate. The next buffer solution in the series can now be applied and the process is repeated.

3.5 Data Processing

The force data obtained from the AFM is raw, unprocessed data. The recorded data are scanner height and cantilever deflection. These must be zeroed and converted to more sensible parameters, separation and force. The separation distance may be determined from the region of constant compliance, or the region where the cantilever no longer indents the sample; the observed force effectively has an infinite slope when plotted as a function of separation. This region denotes zero distance, but in this case it is where the brush can no longer be compressed (*h* in Figure 3-5). It is important to note that zero distance is not the point where force is first observed, but the point where the cantilever is no longer able to compress the sample. Deflection can be converted to force using the spring constant of the cantilever (force is deflection multiplied by the spring constant). This parameter is typically provided by the manufacturer but can also be measured.

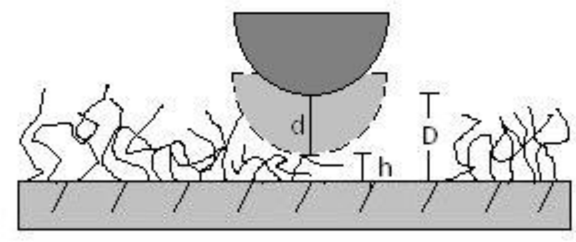

Figure 3-5 – This diagram depicts the parameters d, h, and D, and how D=d+h.

MatLab scripts were used to zero and calibrate the force curves obtained in this experiment. After the data was processed in MatLab, it was imported into Microsoft Excel to convert from deflection to force and to resolve any errors in zeroing. All processed force curves for each pH condition are then averaged to minimize the effects of noise and unique events. This was done in Excel by summing forces and separations for each curve, and dividing by the number of curves summed. The result is a much cleaner force curve which is easier to fit. This also reduces the error in fitting caused by the sinusoidal effects of noise.

The experimental data can now be modeled according to the theoretical force equations. Many different programs are capable of fitting power-law equations to data, but the programs used were MatLab (curve-fitting toolbox), Table Curve, and Excel. MatLab and Table Curve have automatic fitting functions, but Excel is not capable of fitting to the same degree. Instead, Excel was used to manually manipulate the unknown parameters in order to find a fit. Excel was used primarily because it could be forced to fit data while automated fitting programs will produce errors if they are unable. The time constraints of the experiment would not permit extensive effort in fitting the data.

The following equations are force models for different tip geometries adapted from the Alexander-de Gennes surface face apparatus equation for two planes with polymers (Equation 2.5 from Literature Review):

$$F_{sphere} = \frac{8\pi k_B TRL}{35s^3}\left[7\left(\frac{L}{d+h}\right)^{5/4} + 5\left(\frac{d+h}{L}\right)^{7/4} - 12\right] \qquad (3.1)$$

$$F_{pyramid} = \frac{128k_B TL^2}{385s^3}\tan^2\theta\left[77\left(\frac{L}{d+h}\right)^{1/4} + 33\frac{d+h}{L} - 5\left(\frac{d+h}{L}\right)^{11/4} - 105\right] \qquad (3.2)$$

$$F_{cone} = \frac{32\pi k_B TL^2}{385s^3}\tan^2\theta\left[77\left(\frac{L}{d+h}\right)^{1/4} + 33\frac{d+h}{L} - 5\left(\frac{d+h}{L}\right)^{11/4} - 105\right] \qquad (3.3)$$

A derivation of these equations can be found in Appendix A. The desired unknowns are *s*, *L*, and *h*, but *s* is of the most interest. This change of this parameter with different buffer solutions will allude to the validity of the root spacing theory. In the latter two equations, θ is the half-angle of the pyramid or cone.

A study performed by Chang et al. [18] described the effect of pH on polymer conformation. They found that an increase in pH resulted in a relaxation of the polymers as show in Figure 5.2.

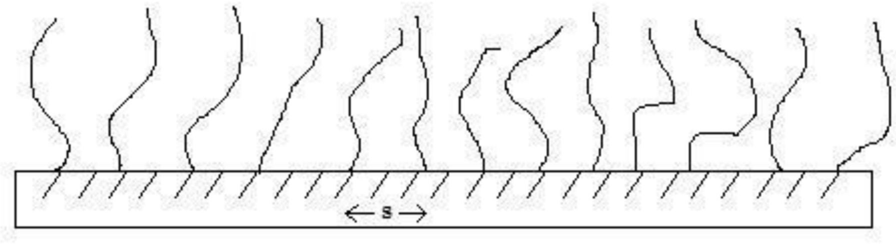

Figure 3-6 – A relaxed polymer brush where *s* is considered to be the root spacing.

Figure 3-6 also shows the perceived root spacing theory. This theory may be more correct in the situation similar to what is depicted above because the density that is "felt" by the AFM tip is very close to the root spacing density. However, in a more condensed brush, such as conditions observed at low pHs, this is not true. Figure 3-7 depicts a condensed polymer brush.

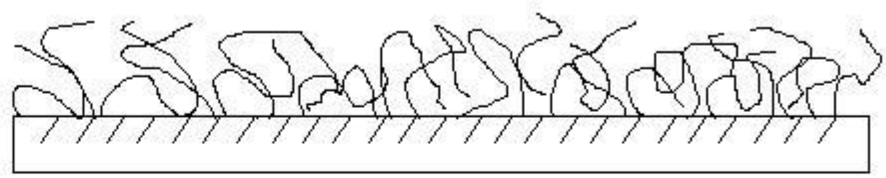

Figure 3-7 – A condensed polymer brush. In this condition it is illogical to assume the force depends on root spacing.

In this case, it would seem as if the root spacing were irrelevant to the force observed by the AFM tip. Instead, the distance between polymer cross-overs would seem more appropriate. Figure 3-8 shows an example of an overlap that may be seen in Figure 3-7. The mesh-spacing is the average spacing between overlaps in the polymer brush.

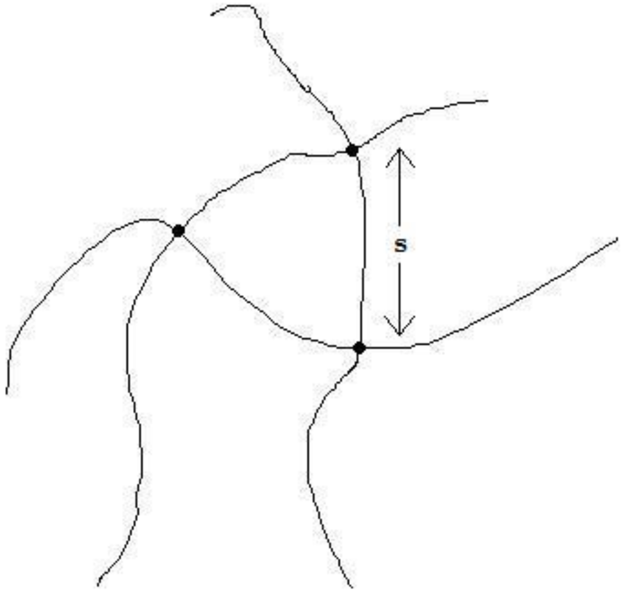

Figure 3-8 – A bird's-eye diagram of what is meant by polymer mesh spacing. These polymer overlaps are most likely observed in low pH conditions where the polymer brush is condensed.

The manipulated variable in this experiment is the pH of the buffer solution; this allows for a condensation and relaxation of the polymer brush. Because of this ability, the correct theory can be selected by data analysis. Experimental data can be fitted over a series of varying pHs, and if the determined value for *s* changes with pH, the mesh-spacing theory can be assumed. In order for the root-spacing theory to hold, the value of *s* must be invariant under a change in pH.

An efficient visual aid of this effect can be made with semi-log plots. The arithmetic involved in doing so can be found in Appendix A. The result of this is a semi-log plot in which its curves have different characteristics depending on the variables *L*, *s*, and *h*. An example plot with the important characteristics can be found in Figure 5.5.

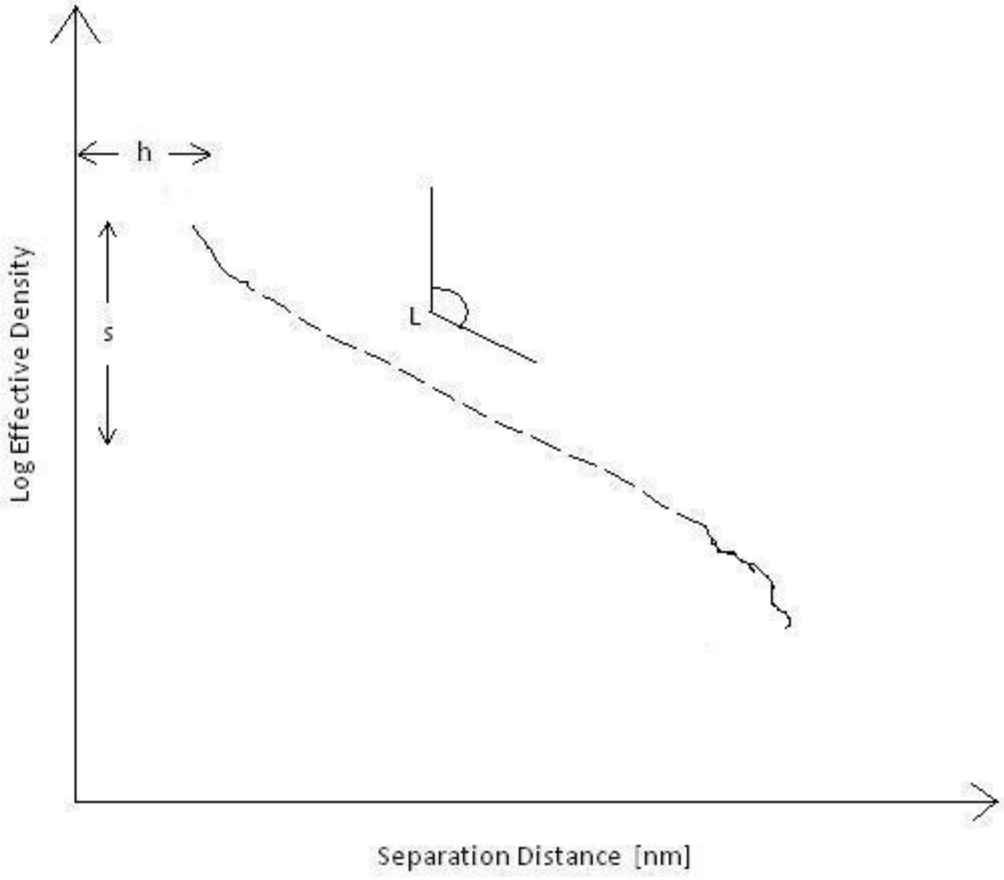

Figure 3-9 – A semi-log plot of force and separation distance used to easily visualize the objective of the experiment.

A typical power-law follows the form of expression seen in Figure 3-9 in a semi-log plot. The shape of this plot is affected by the three variables of interest, *L*, *s*, and *h*. The equilibrium brush thickness, *L*, affects the slope of the dashed region of the semi-log plot. The offset, *h*, affects the horizontal position of the plot. The effective density, *s*, affects the vertical position of the plot. If several plots under different pH conditions are overlaid, it will be easily seen what *s* really is. For *s* to be the root spacing, all plots would have the same y-intercept. This plot is the ultimate representational product of the experiment.

3.6 Imaging Layer Thickness

Several different methods were used in an attempt to image the thickness of the alginate layer on the glass slide. The advantage of doing so would eliminate, or provide a better understanding of one of the unknown variables from the force model, *L*. The two most promising methods are shown here. Other attempted methods can be found in Appendix C.

The first method solves the impracticality of finding the boundary between glass and alginate (see Appendix C) by using the AFM probe to scrape the alginate off the slide. This can be done by starting with a smaller scan size, 1-10 µm, and increasing the gain and set point of the cantilever in contact mode for a small image then increasing the scan size about ten times the previous for another image. Figure 3-10 depicts the ideal result of such a procedure: a small square area without alginate within a larger image.

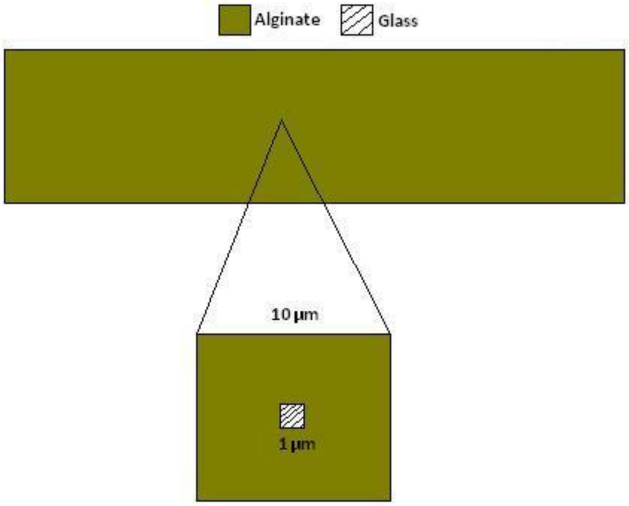

Figure 3-10 – The indent method. The AFM tip is used to indent or scratch the alginate off the surface.

The second method involves the use of a razorblade to scratch or scrape alginate from the surface (Figure 3-11). For the scratch method, the razorblade is dragged perpendicular to the slide in order to produce a thin slice in the layer. This can be done several times and in different orientations to make the process of finding the scratches easier. One caveat of using a razorblade is that it is possible to scratch more than the alginate and actually mark the slide. This would provide a larger measurement of the layer thickness than reality, and could possibly be a significant error.

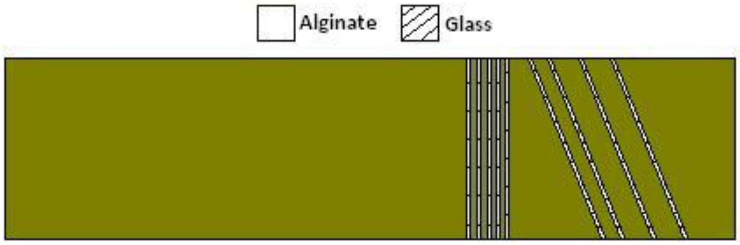

Figure 3-11 – The scratch method. A razorblade is used to scratch a thin line of alginate off the surface.

4 Results and Discussion

The data obtained suggest that *s* is the mesh spacing instead of the root spacing. The general results agreed with the original presumptions that the equilibrium brush thickness, *L*, and *s* would increase as a function of pH, but it is somewhat unclear why *h*, the offset distance, also increased with pH. Further research is needed to make this experiment quantitative, and some suggestions can be found in Section 4.4 – Future Research. It was also consistently apparent that the spherical tip geometry provided the best fit for the data.

4.1 Force Curve Data Fitting

Fitting was attempted in Excel and Table Curve, but Excel and Table Curve did not agree in their fitting. The Table Curve data is not shown because we are unsure of how it calculates error, so only Excel fitting will be shown. The Table Curve data, as well as a comparison between it and Excel, can be found in Appendix C.

Excel was used to manually adjust parameters to fit the experimental data. The fit was done in a linear plot and optimized by minimizing the average percent standard deviation. The percentage standard deviation is calculated as follows:

$$\delta = \left(\frac{F_{exp}}{F_{model}} - 1\right)^2, \qquad (4.1)$$

$$\sigma_{avg} = \sqrt{\sum_{n=1}^{N} \frac{\delta_n}{N}}, \qquad (4.2)$$

where *N* is the number of data points in the force curve, and *n* is the nth data point in the series. This average standard deviation can then be converted to a percentage by multiplying by 100.

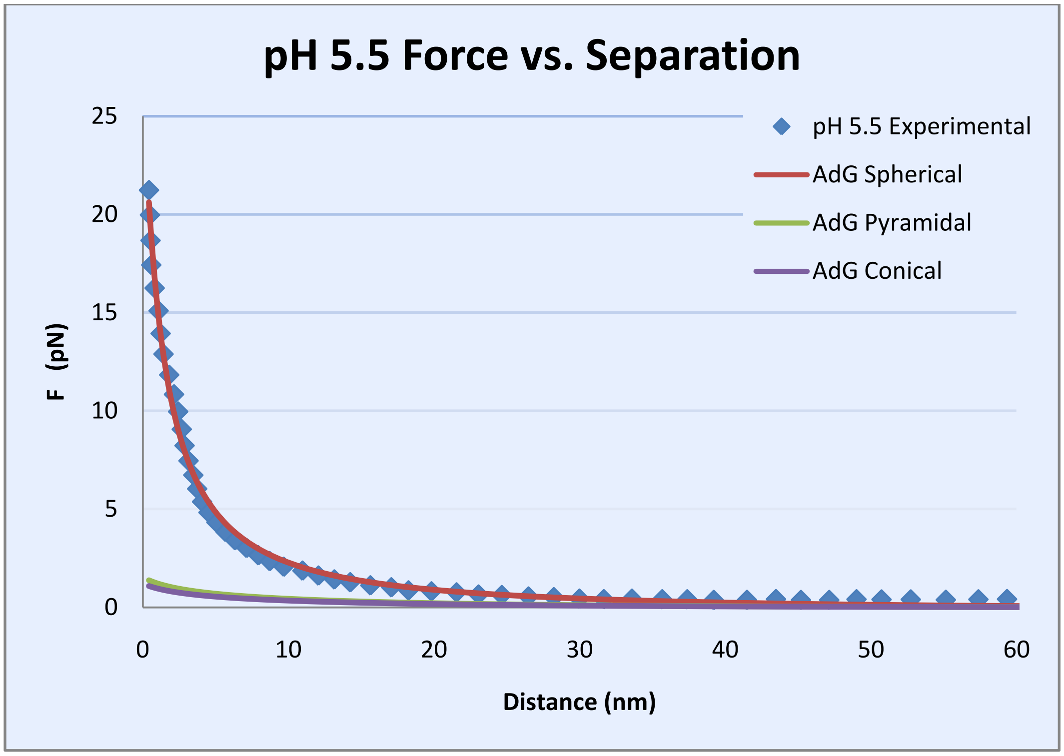

Figure 4-1 – Excel pH 5.5 force vs. separation plot used to fit model to data. The parameters obtained by this fit are 90, 140, and 1.8 nm for s, L, and h. The standard deviation percent error is 24%.

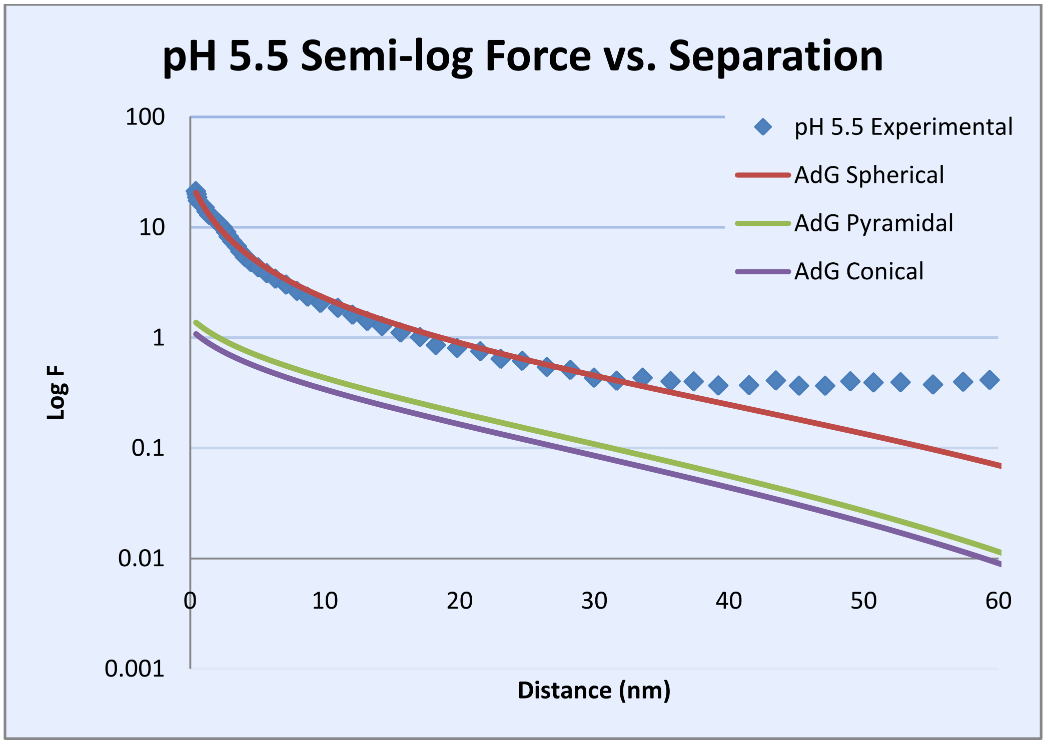

Figure 4-2 – Excel pH 5.5 semi-log force vs. separation plot used to fit model to data. The parameters obtained by this fit are 90, 140, and 1.8 nm for s, L, and h. The standard deviation percent error is 24%.

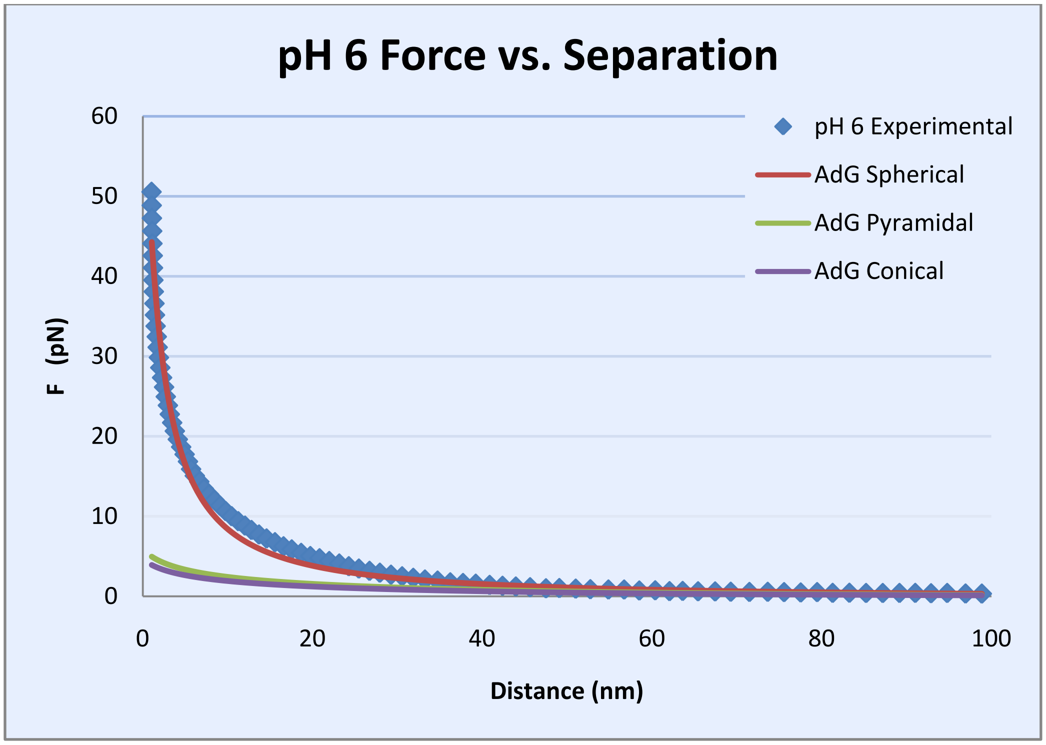

Figure 4-3 – Excel pH 6 force vs. separation plot used to fit model to data. The parameters obtained by this fit are 100, 300, and 3.85 nm for s, L, and h. The standard deviation percent error is 23%.

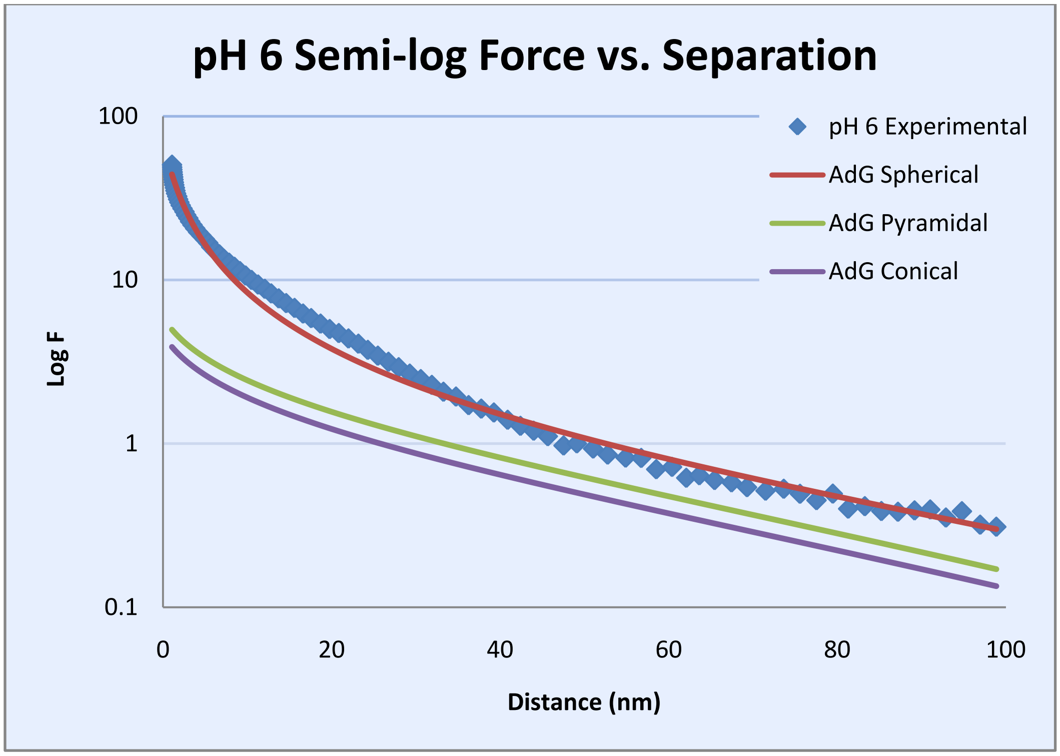

Figure 4-4 – Excel pH 6 semi-log force vs. separation plot used to fit model to data. The parameters obtained by this fit are 100, 300, and 3.85 nm for s, L, and h. The standard deviation percent error is 23%.

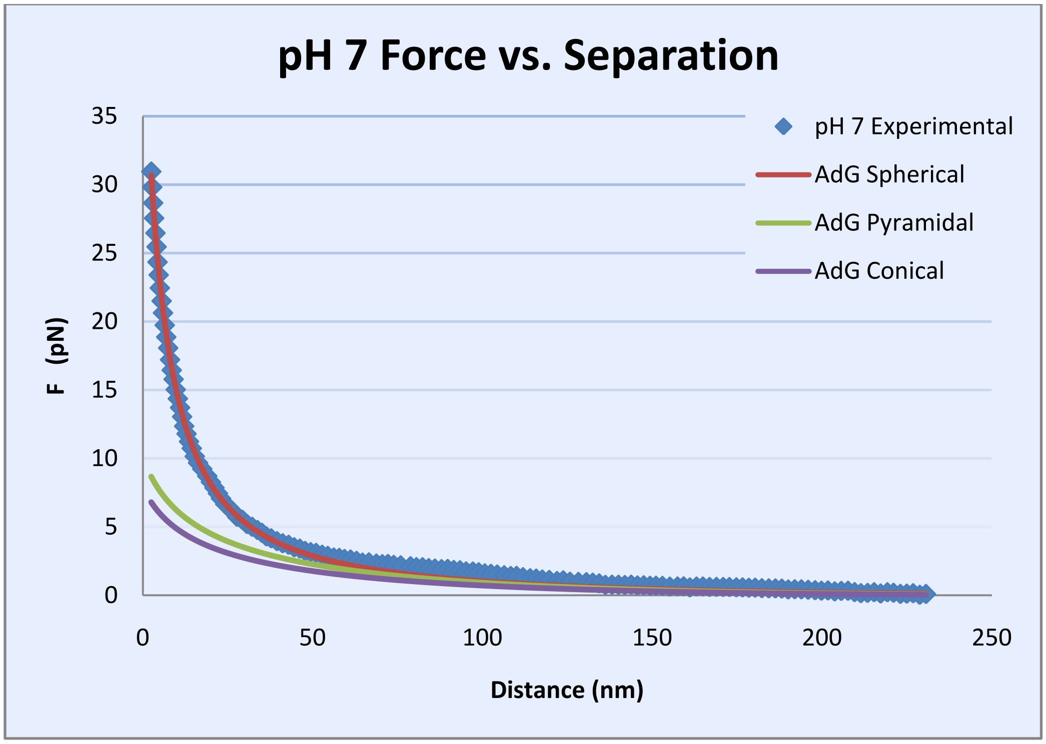

Figure 4-5 – Excel pH 7 force vs. separation plot used to fit model to data. The parameters obtained by this fit are 110, 475, and 10 nm for s, L, and h. The standard deviation percent error is 18%.

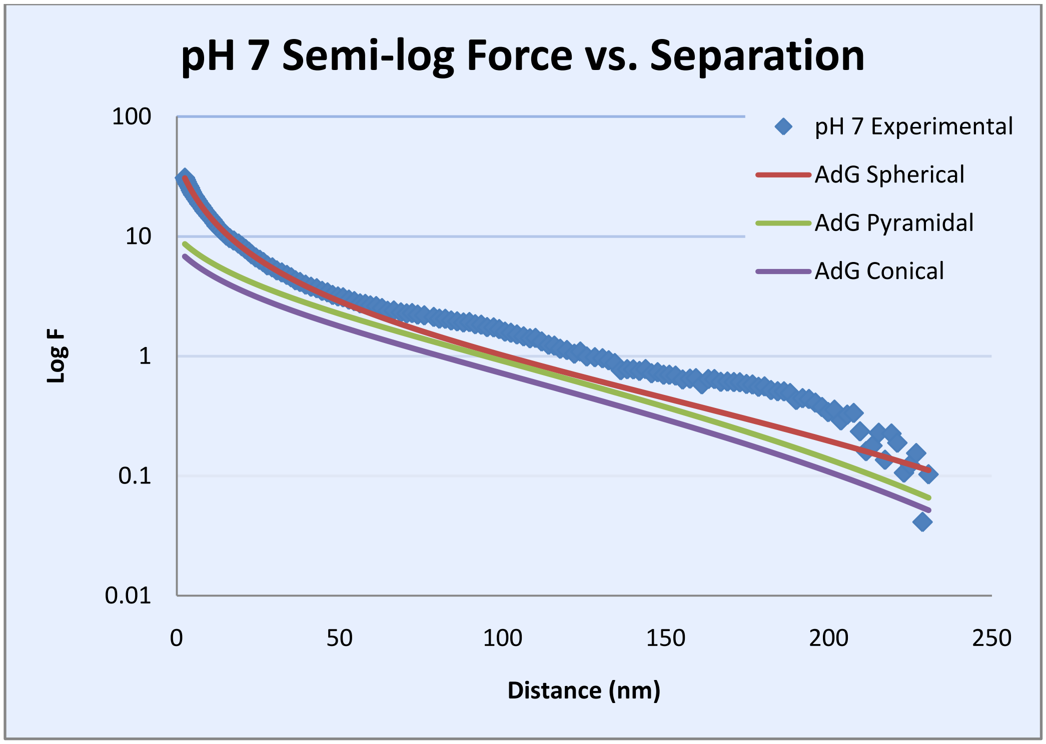

Figure 4-6 – Excel pH 7 semi-log force vs. separation plot used to fit model to data. The parameters obtained by this fit are 110, 475, and 10 nm for s, L, and h. The standard deviation percent error is 18%.

Table 4-1 – Summary of Results for Excel Fitting.

(nm)	**pH 5.5**	**pH 6**	**pH 7**
s	90	100	110
L	140	300	475
h	1.8	3.85	10
Std Deviation %	24	23	18

Excel ended up working very well although it was not able to automatically fit the experimental data. A summary of the parameters obtained from the fitting can be found in Table 4-1. All of the obtained parameters seem to be logical, and *L* and *s* followed the original presumptions of the experiment. Averaging the force curves ended up being extremely helpful in fitting the pH 5.5 condition because most of the individual force curves had a sharp increase to an infinite slope which made the curve difficult to accurately fit. The percentage standard deviation was limited to an average of 21.7% which seemed to produce a good fit.

One major issue when fitting with Excel is obtaining the correct parameters. The effects of changing *s* can be offset by changing *L* and vice versa. This means you could obtain different an opposite configuration of the *L* and *s* parameters with close to the same error. The trick to solving this problem is to watch the semi-log plot while choosing parameters. It is important to first choose a value for *L* that causes the theoretical curve to approximate the slope of the experimental data. This appears to be somewhat difficult if the data is noisy, or begins to curve up as seen in Figure 4-1 and Figure 4-2. The most important region to fit is the exponential data in the linear plot or the data closest to zero separation. This is the most interesting region of the entire force curve because it is where the polymer brush primarily interacts with the AFM tip. It will also be the most accurate data in the curve because sometimes Matlab has difficulty zeroing the raw force curve and as separation distance increases the curve may tend to curl up away from zero. This also enforces the necessity of trimming the data used in the fitting—extra data outside of the region of interest serves little purpose, and the extent of the data used should be carefully considered.

4.2 Results

4.2.1 Individual vs. Averaged Force Curves

The averaging of force curves greatly helped the fitting of the data. It effectively eliminated a majority of the noise that was observed, and allowed for easier fitting of the exponential regime. However, there are some questions as to the legitimacy of this process. Figures 2.1 and 2.2 are shown to compare the individual and averaged force curves. It seems as if the pH 5.5 curve was affected the most from the averaging, and it is questionable if the averaging changed the data and observed behavior of the brush. This is something which needs further investigation. It may have been better to not average the pH 5.5 data, although the averages from pH 6 and 7 do not appear to have been altered as much.

A potential caveat in averaging is the effect of thermal drift. Thermal drift is an expanding caused by temperature changes in the room. This temperature change is primarily a result of the AFM machinery. If there was significant thermal drift throughout the duration of force curve acquisition for a single condition, the averaging process would no longer be valid. It may be more acceptable if the force curves were taken in rapid succession and in multiple regions of the brush. Force curves for this experiment were typically taken in two separate regions of the slide in an attempt to obtain average parameters (assuming the brush is not completely homogenous).

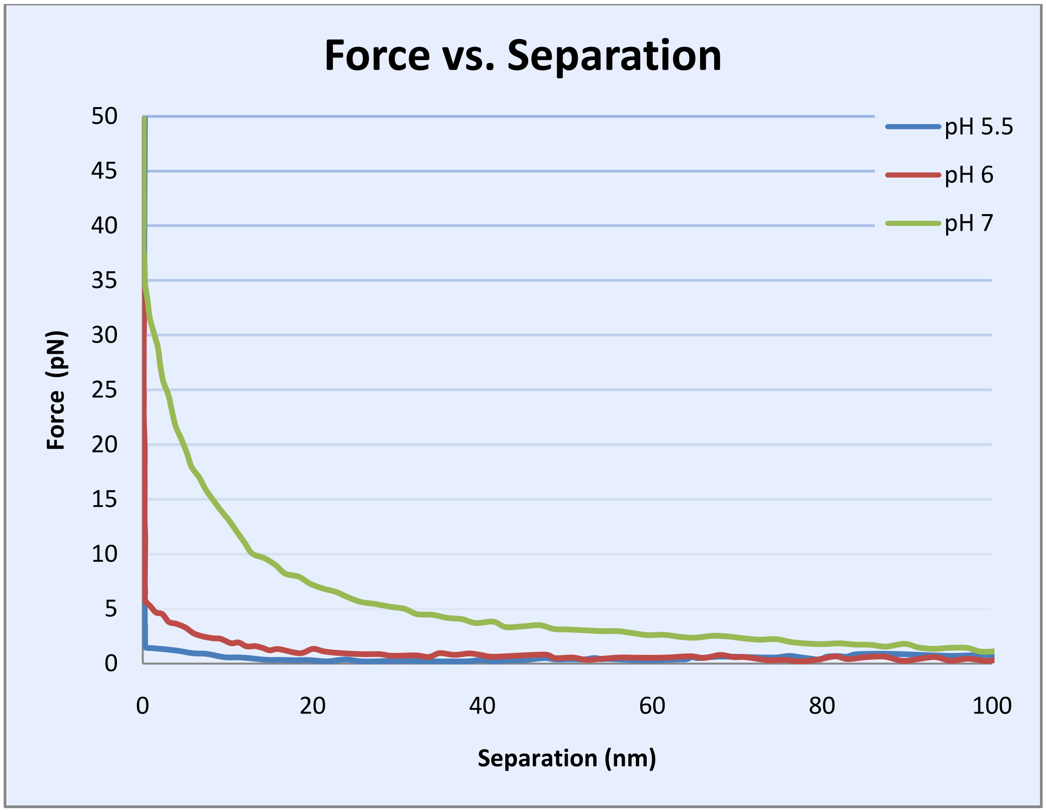

Figure 4-7 – Individual force curves from a single trial.

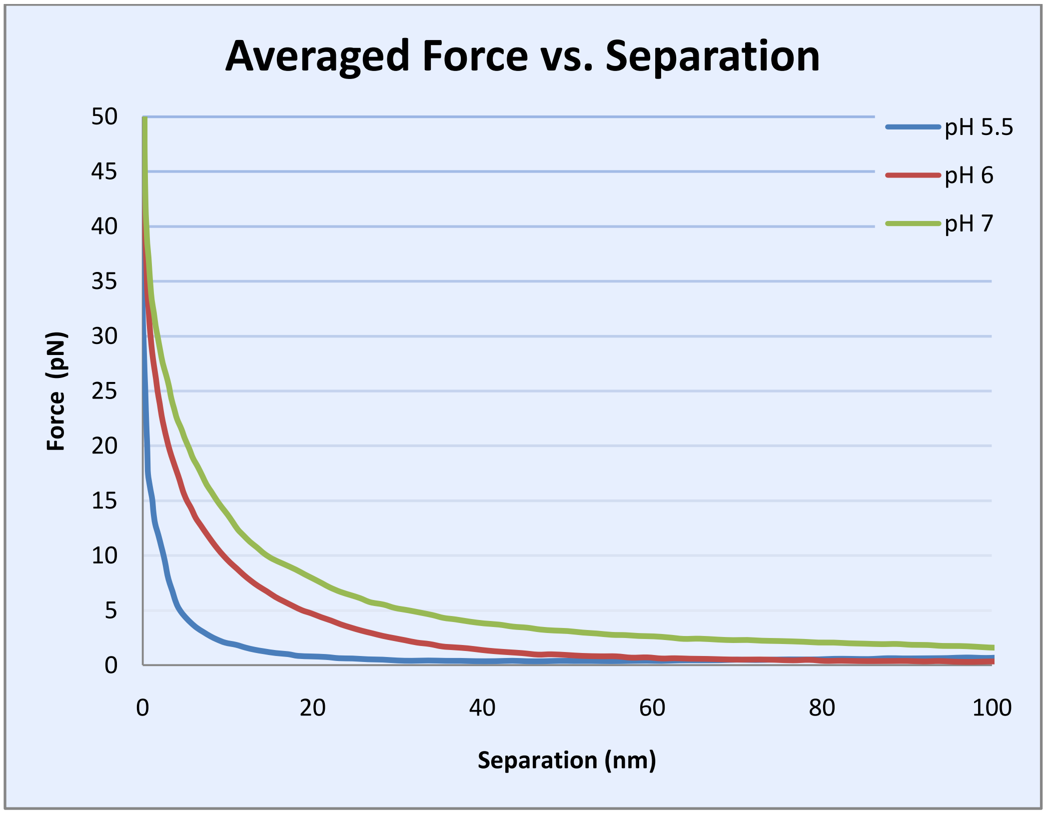

Figure 4-8 – Averaged force curves from a single trial.

Another concern is the disappearance of the kink in the pH 5.5 curve from Figure 4-7 in Figure 4-8. It is something that needs investigation—perhaps of the legitimacy of the averaging.

4.2.2 Semi-log Effective Density

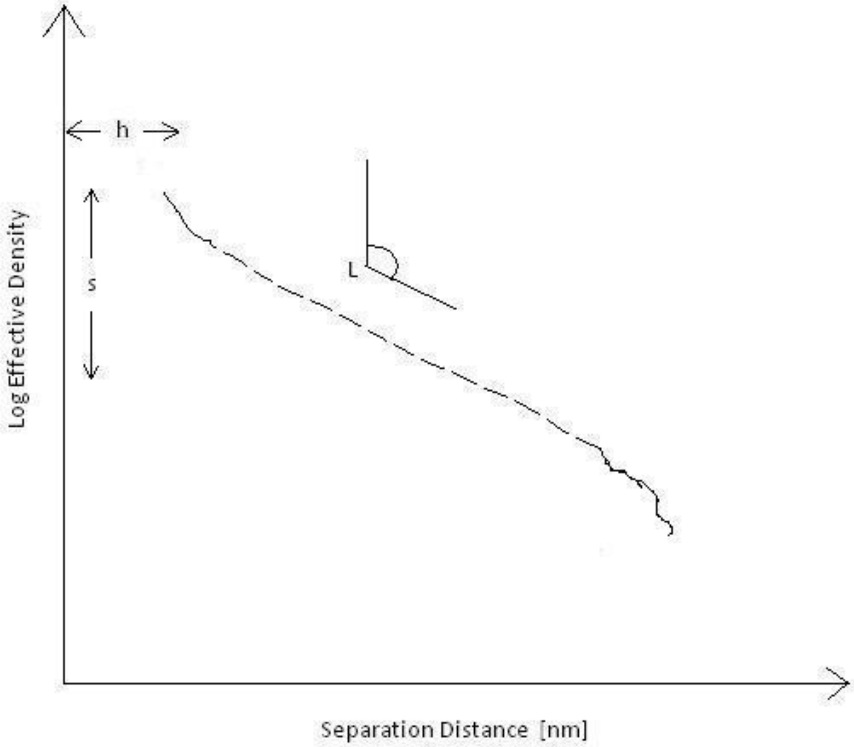

Figure 4-9 – A semi-log plot of force and separation distance used to easily visualize the objective of the experiment.

Figure 4-10 is the final product of this experiment. It is the semi-log effective density plot explained in the Data Processing section of the Experimental chapter and Figure 4-9. It is clear by these plots that all parameters at least changed under pH variation. Although the Table Curve data was not in accordance with the original presumptions (*s* did not consistently increase with pH), it still supports the mesh spacing hypothesis because the value for *s* was different in each condition. The effective density plot corresponds with the presumptions that *L* and *s* would increase with pH. The fits in these plots may look somewhat inaccurate, but this is primarily a side effect of semi-log plots—they exaggerate small discrepancies in linear plots. The lower pH data is also less exponential and therefore harder to fit.

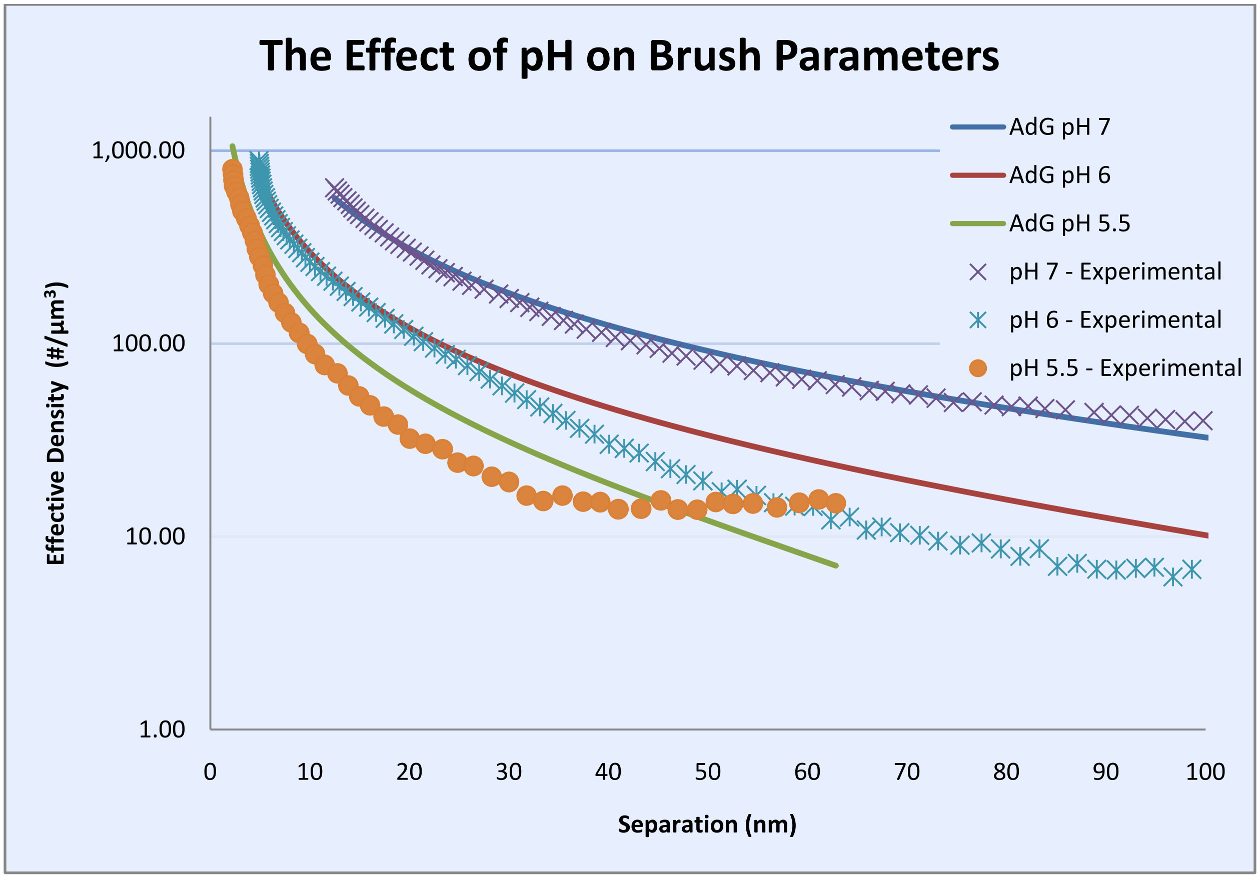

Figure 4-10 – Excel effective density plot demonstrating how brush parameters change with pH.

4.2.3 Summary of Results

Figure 4-11 shows numerical and visual brush trends as a function of pH. The data shown is obtained from the Excel fitting because it was chosen to have the best fit. All parameters were found to increase with pH according to our original presumptions.

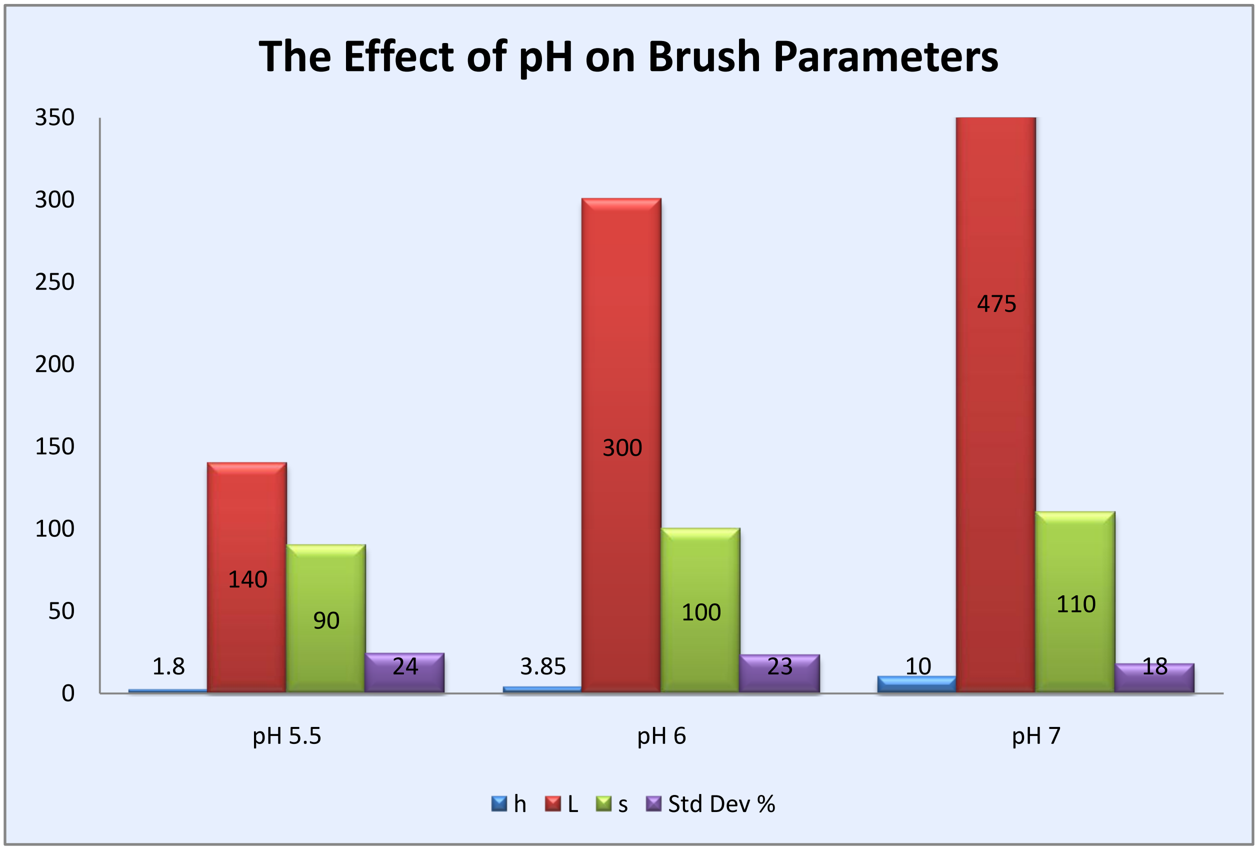

Figure 4-11 – The trends seen in brush parameters as pH is increased (Excel).

4.3 Conclusion

Although Excel and Table Curve did not agree on the brush parameters for each condition, and Table Curve did not agree with some of the original presumptions of the experiment, they agreed with the hypothesis that *s* would change under pH variation. This is the most important result of the experiment. This data certainly suggests that *s* is *not* the root spacing, but some sort of mesh spacing. Of course, further research is needed in order to become more quantitative and influential. There are several relatively simple improvements to be made which were outlined in the previous section and could greatly improve the results. This experiment appears to be a success in-as-far as the data suggest.

4.4 Future Research

There are several improvements that could be made in the future to make this experiment more successful. They will be discussed in order of their potential impact on the experiment.

4.4.1 Finding the Equilibrium Brush Thickness Experimentally

The first, easiest, and most beneficial improvement to be made would be to image the polymer layer height experimentally. Two possible methods for doing so are discussed at the end of the experimental chapter of this report. Some other techniques that were attempted can be found in Appendix C. Obtaining *L* in this manner would eliminate one of the three variables that need to be fit. This would provide much higher accuracy in the extraction of *s* and *h* and would allow for automatic fitting in Excel. It would also most likely make any sort of automatic fitting much less troublesome. Of course, whatever method that was used would have to be done in each pH condition to obtain their respective value for *L.* It would also be of benefit to find the layer height in several different areas on the slide to ensure the homogeneity of the brush.

4.4.2 Increased pH Buffer Variation

Another relatively easy improvement would be to use a greater variation of pH, and possibly more discrete pH variation in order to observe more of a consistent trend. It should be noted that pHs below 5.5 become extremely difficult to fit because of their force curve's abrupt change in behavior. The effectiveness of the EDC/NHS binding also needs to be investigated at pHs above 7, because it is possible that the bond formed becomes loose or brittle in more basic solutions. As for the size of the deviations between pH conditions, they should probably be no smaller than 0.25 or 0.3 for sake of time (all force measurements for a trial should be taken in one sitting) and the differences could start to blur. However if time was not an issue, very discrete variations could produce an effective visual (similar to the one seen in Figure 3.1)—although the individual variations between the steps may not be consistent with presumptions, the overall trend would be influential. Perhaps a function of mesh spacing's dependence on pH could even be determined experimentally for different polymer brushes.

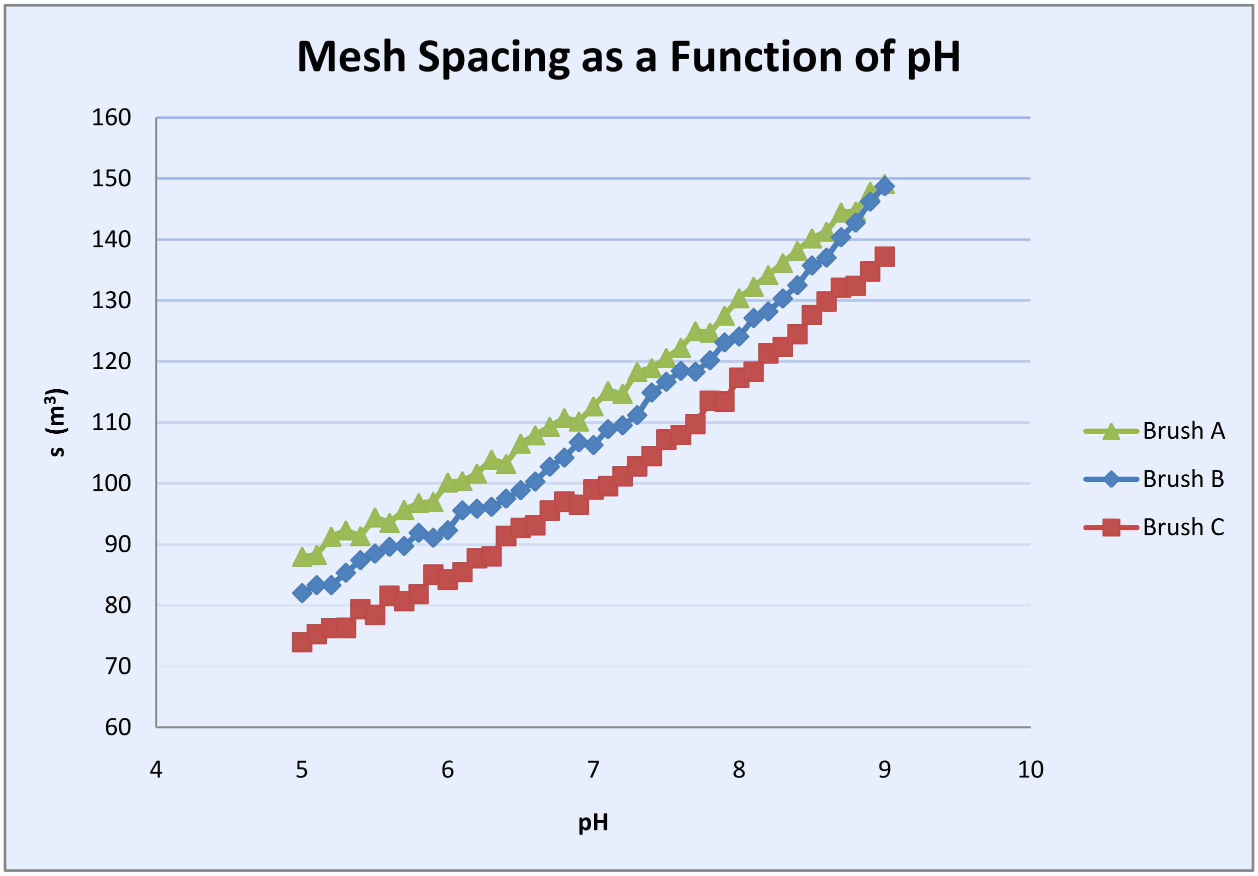

Figure 4-12 – A potential investigation of the mesh spacing's dependence on pH.

4.4.3 Keeping the Sample Wet During pH Variation

Another potential problem with the polymer brush is that it could be drying too much while the buffer solution is being switched. This could cause the polymers to constrict to the slide and distort the subsequent force curves that are taken in the next buffer. One way to test for this would be to take force curves only at a certain pH, and then again after varying pH a few times. Some solutions to this problem, if it is a significant one, are to one, have separate slides for each pH, or 2, continuously vary the pH buffer by keeping the slide in a bath where the buffer solution is continuously fed through the bath. One would have to have some way of ensuring the slide had enough time to soak in the new pH buffer before taking force measurements for the latter method to be effective.

4.4.4 Better Fitting of Data

One crucial step that was abandoned because of time constrains was the use of better fitting programs and the use of several different programs to reaffirm the fitted parameters. The most intricate of the fitting programs that were explored was the Matlab Curve-Fitting toolbox, a separate extension of Matlab which has the ability to fit complex data with many variables. This fitting program would have certainly provided the most reliable fits and probably uses the most sophisticated fitting algorithm of any program. The use of multiple programs is also reassuring if they obtain the same or similar fitting parameters. The accuracy of fitting in a semi-log plot should also be investigated. And the legitimacy of averaging force curves also needs attention. Temperature changes in the room should be noted during force curve acquisition, and perhaps a study should be conducted to examine the extent of thermal drift that occurs and its effect on averaging.

4.4.5 Spherical AFM Probes

The use of spherical AFM probes with large radii, known as colloidal probes, would be a good improvement because the tip would better match the geometry that the spherical model was derived for. The large radius would also measure a greater area of interaction, and therefore give more average parameters when fitted. One problem with the way the models were derived was that they don’t perfectly reflect the physical situation. This is because the AFM cantilever actually comes down at an angle, so the tip enters the brush asymmetrically. The models do not account for this type of interaction, but a spherical tip is symmetrical even when rotated about an angle. In this way the spherical model is superior to the other two, and would be the best approximation if truly spherical probes were used.

4.4.6 Better Replication of Bacterial Brush

Alginate was used to model the bacterial brush in this experiment, and some potential caveats of its use were outlined in the Alginate section of the Literature Review chapter. Prima facie, the alginate prefers no particular conformation on the glass slide, and may bind in any which way. This could mean that the alginate binds along its axis and just lays flat on the slide. This is not the ideal conformation for modeling a bacterial brush where the polymers are believed to have a single binding site on the cell and more or less stand up straight. A diagram of what could be happening is shown in Figure 4-13.

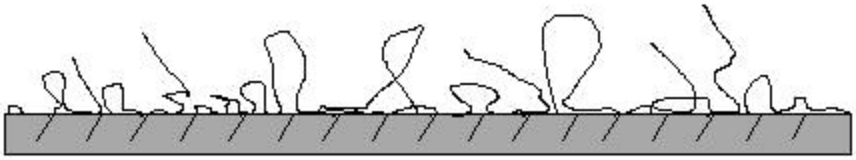

Figure 4-13 – A scenario where the alginate binds indiscriminately to the glass slide.

This condition is not necessarily a terrible model for a bacterial brush, because it could still present similar forces to what would be seen in the ideal bacterial brush. It is somewhat unclear how the looping and multi-binding is different from the ideal case. The biggest fallacy that could come from what is seen in Figure 4-13 is our conclusions concerning the meaning of *s*. It is possible that the model with alginate could obscure the results because of the way it binds to the slide.

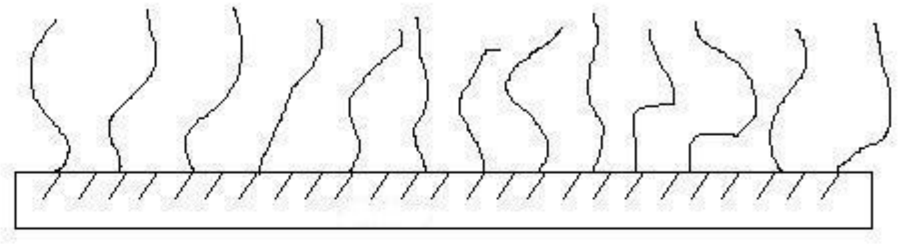

Figure 4-14 – The ideal model of a bacterial brush. Each polymer has only one binding site on the glass slide.

Figure 4-14 depicts the ideal model for a bacterial brush. The ideal model would have each polymer only binding once to the slide so that something like what is seen in Figure 4-14 would be more likely to occur. Also note that this diagram depicts the brush in a higher pH, and that the polymers would still conform differently in the presence of varying pH buffers. One alternative model was found long after alginate was chosen. This model uses diblock copolymers, or a polymer with a "block" molecule on each end. One of these blocks is easily absorbed by the substrate and the other is not. The second block causes the polymer to be extended out into the solution. There are also several other journals describing this method (see references 9-14 in [17]).

4.4.7 More Quantitative Consideration

The final steps to be taken towards more accurate data, is first to obtain more of it, and then after all other considerations have been taken and quantitative data can be trusted, to experimentally measure the cantilever stiffness of spring constant k_c, and the tip radius R. These parameters can be measured using certain AFM techniques [30]. In many cases, the manufacturer's nominal or maximum values are far different from the measured values if the tips have been used. For this reason, it is important to measure the stiffness of the cantilever and tip radius experimentally in order to achieve accurate parameters. The manufacturer supplied values were used for the purposes of this experiment because it was not yet at a stage where numbers could be trusted anyways—the focus was to observe trends.

4.4.8 Investigation of Matlab Scripts

The Matlab scripts that are used to convert the raw AFM force curves (scanner position vs. cantilever deflection) need to be investigated in order to ensure the conversion process is acceptable. Some of the force curves have come out of Matlab processing with puzzling features and unreasonable calibration error. For example, some curves have appeared to have little noise, but come out of Matlab with exaggerated noise, or appear to have been rotated in such a way that the force increases at large separations. It would seem as if there could be an error in the zeroing process.

5 References

[1] U. S. G. Survey, 2008.
[2] D. Davis, 2007.
[3] A. B. Cunningham, J. E. Lennox, and R. J. Ross, Vol. 2008-2009, erc.montana.edu, 2008.
[4] R. C. W. Berkeley and S. o. C. Industry, Microbial adhesion to surfaces, Published for the Society of Chemical Industry distributors, Halsted Press, Chichester New York, 1980.
[5] A. Atabek, Y. Liu, P. A. Pinzon-Arango, and T. A. Camesano, Colloids and Surfaces B-Biointerfaces 67 (2008) 115.
[6] J. W. Costerton, P. S. Stewart, and E. P. Greenberg, Science 284 (1999) 1318.
[7] M. R. Parsek and C. Fuqua, J. Bacteriol. 186 (2004) 4427.
[8] D. C. Savage and M. Fletcher, Bacterial adhesion : mechanisms and physiological significance, Plenum Press, New York, 1985.
[9] J. W. Costerton, Z. Lewandowski, D. DeBeer, D. Caldwell, D. Korber, and G. James, J. Bacteriol. 176 (1994) 2137.
[10] A. H. Rickard, P. Gilbert, N. J. High, P. E. Kolenbrander, and P. S. Handley, Trends in Microbiology 11 (2003) 94.
[11] M. C. Walters, III, F. Roe, A. Bugnicourt, M. J. Franklin, and P. S. Stewart, Antimicrob. Agents Chemother. 47 (2003) 317.
[12] I. Keren, D. Shah, A. Spoering, N. Kaldalu, and K. Lewis, Journal of Bacteriology 186 (2004) 8172.
[13] B. W. Ninham, Advances in Colloid and Interface Science 83 (1999) 1.
[14] M. Hermansson, Colloids and Surfaces B: Bionterfaces 14 (1999) 105.
[15] M. Bostrom, D. R. M. Williams, and B. W. Ninham, Physical Review Letters 8716 (2001)
[16] P. G. Degennes, Advances in Colloid and Interface Science 27 (1987) 189.
[17] H. J. Butt, M. Kappl, H. Mueller, R. Raiteri, W. Meyer, and J. Ruhe, Langmuir 15 (1999) 2559.
[18] D. P. Chang, N. I. Abu-Lail, F. Guilak, G. D. Jay, and S. Zauscher, Langmuir 24 (2008) 1183.
[19] I. Sokolov, S. Iyer, V. Subba-Rao, R. M. Gaikwad, and C. D. Woodworth, Applied Physics Letters 91 (2007)
[20] S. B. Velegol and B. E. Logan, Langmuir 18 (2002) 5256.
[21] F. Bueche, Physical properties of polymers [by] F. Bueche, Interscience Publishers, New York, 1962.
[22] P. J. Flory, Principles of polymer chemistry, Cornell University Press, Ithaca, 1953.
[23] S. S. Pedersen, N. Hoiby, F. Espersen, and C. Koch, Thorax 47 (1992) 6.
[24] P. P. R. Products, in Instructions (F. 1, ed.), Pierce, Roxford, p. EDC/NHS Reaction.
[25] M. Chaplin, 2008.
[26] V. Instruments, Vol. 2009, Camarillo, CA, 2008, p. DNP.
[27] P. Nanotechnology, Vol. 2009, Pacific Nano, Santa Clara, 2002-2009.
[28] J. Sader, Roland Piquepaille, 2003.
[29] A. W. Decho, Carbohydrate Research 315 (1999) 330.
[30] N. Burnham, in An Introduciton to Atomic Force Microscopy Instrument Lab Instructions, Worcester Polytechnic Institute, Worcester, 2009, p. 7.

6 Appendices

6.1 Appendix A – Derivations

(Thanks to Professor Burnham)

6.1.1 Derivation of the Spherical AFM Force Model

Starting with the Alexander-de Gennes expression for pressure,

$$P = \frac{k_B T}{s^3}\left[\left(\frac{L}{D}\right)^{9/4} - \left(\frac{D}{L}\right)^{3/4}\right]$$

Converting to sphere-flat geometry by

$$F = 2\pi r \int P dr$$

And relating r and z

$$R^2 = \left(R + D - z\right)^2 + r^2$$

$$r^2 \approx 2R\left(z - D\right)$$

$$F = 2\pi \int PRdz$$

And plugging in P

$$F = \frac{2\pi k_B TR}{s^3}\int_D^L\left[\left(\frac{z}{L}\right)^{-9/4} - \left(\frac{z}{L}\right)^{3/4}\right]$$

$$F_{sphere} = \frac{8\pi k_B TRL}{35s^3}\left[7\left(\frac{L}{d+h}\right)^{5/4} + 5\left(\frac{d+h}{L}\right)^{7/4} - 12\right].$$

6.1.2 Derivation of Conical and Pyramidal AFM Force Models

The conical and pyramidal AFM models are derived in the same manner as the spherical equation.

First, the differential area is calculated.

$$da_{pyramid} = 8xdx = 8tan^2\theta(z-D)dz$$

$$da_{cone} = 2\pi rdr = 2\pi tan^2\theta(z-D)dz$$

Then, the AdG pressure equation is integrated over that differential area.

$$F = \int_D^L P(z)da$$

$$\int_D^L \left[\left(\frac{Z}{L}\right)^{-9/4} - \left(\frac{Z}{L}\right)^{3/4}\right](z-D)dz$$

After some arithmetic,

$$F_{pyramid} = \frac{128k_B TL^2}{385s^3}\tan^2\theta\left[77\left(\frac{L}{d+h}\right)^{1/4} + 33\frac{d+h}{L} - 5\left(\frac{d+h}{L}\right)^{11/4} - 105\right],$$

and

$$F_{cone} = \frac{32\pi k_B TL^2}{385s^3}\tan^2\theta\left[77\left(\frac{L}{d+h}\right)^{1/4} + 33\frac{d+h}{L} - 5\left(\frac{d+h}{L}\right)^{11/4} - 105\right].$$

6.1.3 Comparison of Tip Geometries

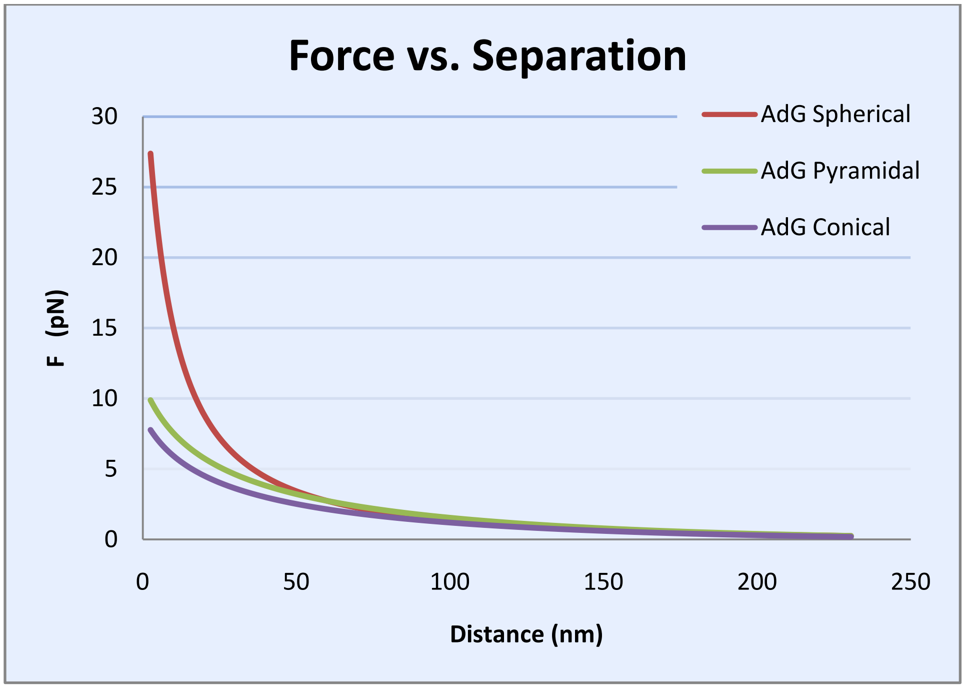

Figure 6-1 – A comparison of the force curves for the derived tip geometries in a linear plot.

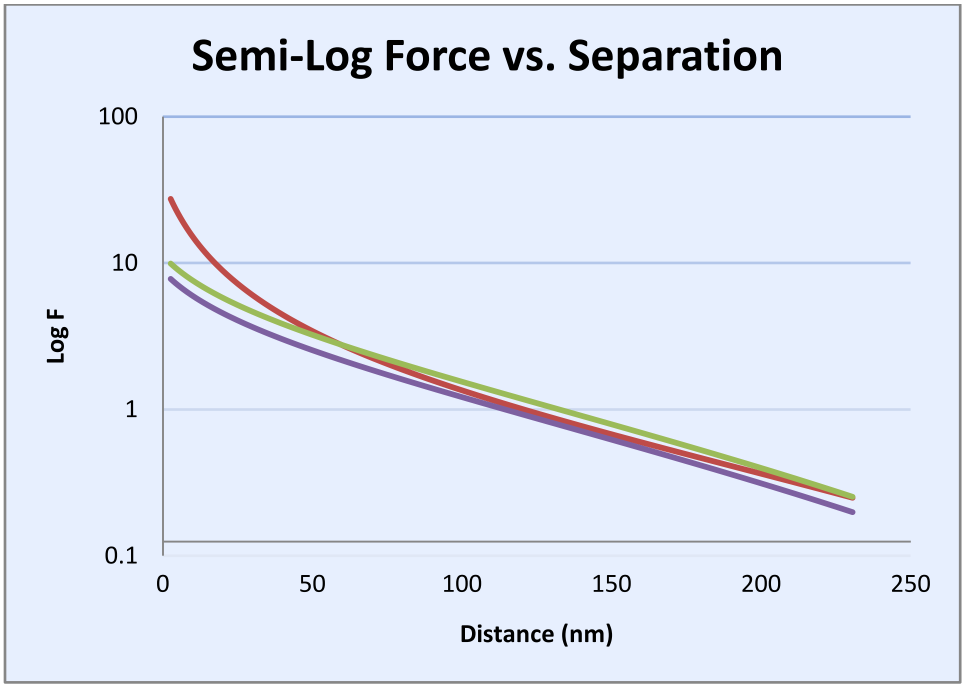

Figure 6-2 – A comparison of the derived tip geometries in a semi-log plot. Note that the same key is used in this plot as in Figure 6-1.

6.1.4 To Convert the Model for Semi-log Plot

First, to simplify arithmetic,

$$\chi_D = \left[7\left(\frac{L}{d+h}\right)^{5/4} + 5\left(\frac{d+h}{L}\right)^{7/4} - 12\right],$$

And

$$\chi_h = \left[7\left(\frac{L}{h}\right)^{5/4} + 5\left(\frac{h}{L}\right)^{7/4} - 12\right].$$

Where χ_D pertains to when the tip is retracted beyond *h* and χ_h is where D=h or d=0. $\chi_D = \chi_h$ at this point.

In order to simplify the plots we normalize the forces

$$\eta = \frac{35F}{8\pi k_B TRL\chi_h} = \eta_0 \frac{\chi_D}{\chi_h},$$

where $\eta_0 = \frac{1}{s^3}$.

Taking the natural log gives

$$\ln\eta = \ln\eta_0 + \ln\frac{\chi_D}{\chi_h}$$

When D=h, d=0 and

$$\chi_D = \chi_h \rightarrow \ln\frac{\chi_D}{\chi_h} = \ln 1 = 0$$

Now we plot $\ln \eta$ against D, if all lines intersect the y-axis at the same point ($\ln \eta_0$) then evidence supports *s* being the root spacing. If the $\ln \eta_0$ varies with ionic strength then evidence supports *s* as the mesh spacing or distance between cross linking polymers.

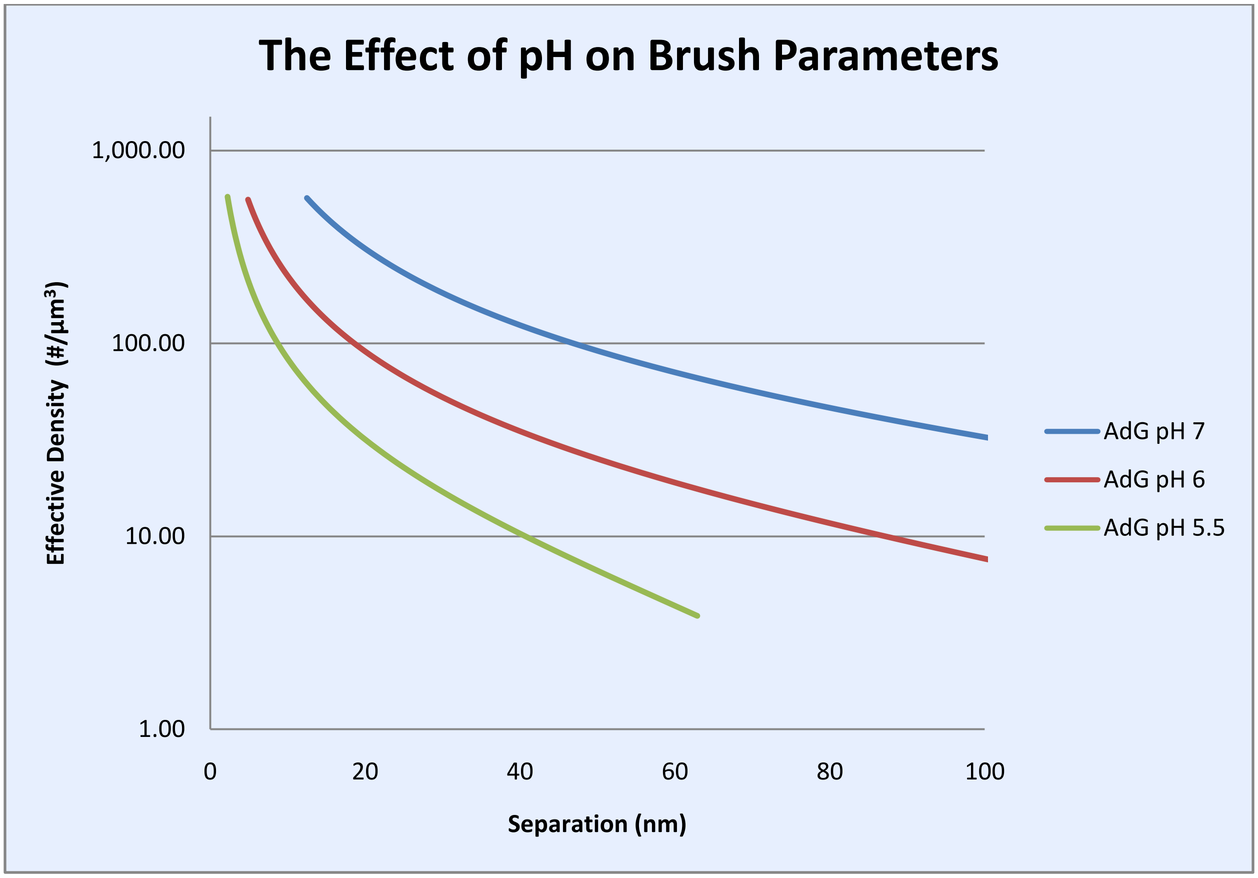

Figure 6-3 – An example effective density plot. The purpose is to visualize brush parameter trends across pH values.

6.2 Appendix B – Procedures and Materials

6.2.1 Cleaning Glass Slides

Plain Corning^{TM} micro slides were used for all experiments. A number of slides were cleaned and stored ahead of time. The cleaning procedure is as follows:

1. Cut slides to desired dimensions (optional).
2. Rinse slides with mili-Q water.
3. Sonicate (Branson 2510 sonicator) slides for 15-30 minutes.
4. Soak in 3:1 HCl/HNO_3 for at least 25 minutes.
5. Rinse with mili-Q water.
6. Soak in 7:3 H_2SO_4/H_2O_2 for about an hour.
7. Keep in ultra-clean water (slides remain clean for about one month).

Before use:

1. Dry slide/s with nitrogen gas.
2. Immerse in ethanol for 5 minutes.
3. Immerse in methanol for 5 minutes.
4. Dry with nitrogen gas.

6.2.2 Alginate Binding

1. Make sure to stir alginate using for at least 20 minutes before binding.
2. Clean the glass slides following the “before use” section of cleaning glass slides.
3. Mix a 9:4 solution of methanol/aminosilane using a mini vortexer (Fisher Scientific) or similar method.

4. Immerse individual slides in solution in Petri dishes for 15-20 minutes.
5. Mix 10 mL of the alginate solution with 300 µL EDC.
6. Incubate the solution at 37°C for 15 minutes while rotating at 18 RPM (the alginate binds to the EDC during this step).
7. Add 600 µL NHS and rotate for 20 minutes at 18 RPM and 37°C (the NHS binds to the EDC during this step, the NHS will later bind to the aminosilane on the glass slide).
8. Leave the solution mixing overnight on a magnetic stirrer (VWR hotplate/stirrer).
9. If not used immediately after mixing, the solution should be mixed again. Let it mix for at least 20-30 minutes before use.
10. Clean the slides with methanol and ultra-pure water and place back in Petri dishes.
11. Immerse slides in alginate solution and set on a rotator at 70 RPM for at least 4 hours.

6.2.3 Complete Materials List

Devices

Atomic Force Microscope *Veeco Dimension 3100*

DNP-S Probes *Veeco*

Mini Vortexer *Fisher Scientific*

Sonicator *Branson 2510*

Rotating Table Mixer *Lab-Line*

Magnetic Stirrer *VWR*

Chemicals

Alginate

N-hydroxysuccinimide (NHS)

1-ethyl-3-[3-dimethylaminopropyl]carbodiimide (EDC)

3-Aminoporpyltrimethoxysilane (Aminosilane) *Aldrich*

Ethanol

Methanol

Mili-Q Water

HCl (Hydrochloric Acid)

HNO_3 (Nitric Acid)

H_2SO_4 (Sulfuric Acid)

H_2O_2 (Hydrogen Peroxide)

NaOH (Sodium Hydroxide)

Nitrogen Gas

KH_2PO_4 *SIGMA* (Potassium Dihydrogen Phosphate)

Diidomethane

Formamide

General Materials

Microscope Slides *Corning*

Petri Dishes

Precision Pipettes

6.3 Appendix C – Failed Trials and Techniques

6.3.1 Imaging the Brush Equilibrium Thickness

The first method devised was to wrap a thin strip of tape around the glass slide prior to any binding. The tape would then be removed before AFM analysis and the area underneath the tape would (ideally) be free of alginate. One of the potential problems here is that the tape leaves a sticky residue behind, and could affect the measurement of the layer thickness. Another practical problem of this method involves finding the boundary between the alginate and where the tape used to be. This can be solved by using a permanent marker to color in the area that the tape fills from the other side of the slide. It may still be difficult, however, to find this boundary with the AFM if the optics are not precise enough. This was the reason this method failed in this experiment.

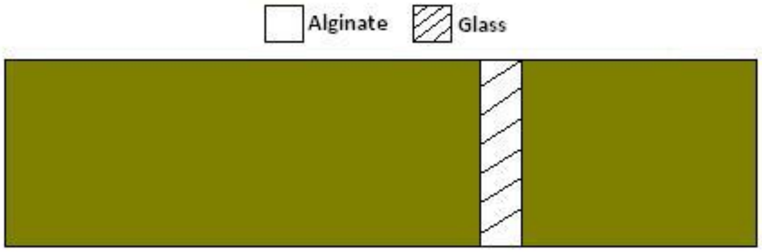

Figure 6-4 – The tape method. Tape is wrapped around the slide before binding and removed before AFM.

The scrape method uses the razorblade to scrape the alginate off parallel to the slide from a certain point. This method is similar to the tape method but resolves the possible residue problem.

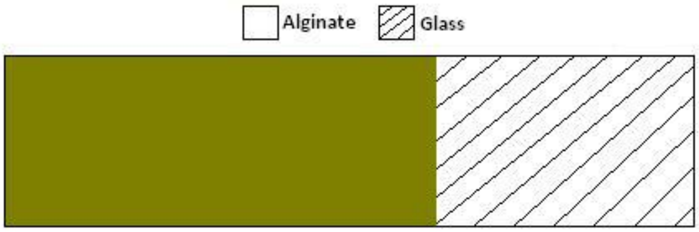

Figure 6-5 – The scrape method. A razorblade is used to scrape the alginate from one side of the glass slide.

A potential source of error when using a razorblade could be that the slide is scratched in the process, and glass is actually removed from the slide. This would result in a larger estimate of the layer thickness than in reality.

6.4 Table Curve Fitting

Table Curve was the first program to automatically fit the data from this experiment. It ultimately provided ball-park estimates for the values of parameters used in the Excel fitting. Table Curve offers a relatively simple user-interface, and the fitting was straight-forward for the most part. Once again, it is important to trim the data used so that the fitting is done primarily on the region of interest. Table Curve has a data exclusion function which makes this process a lot easier.

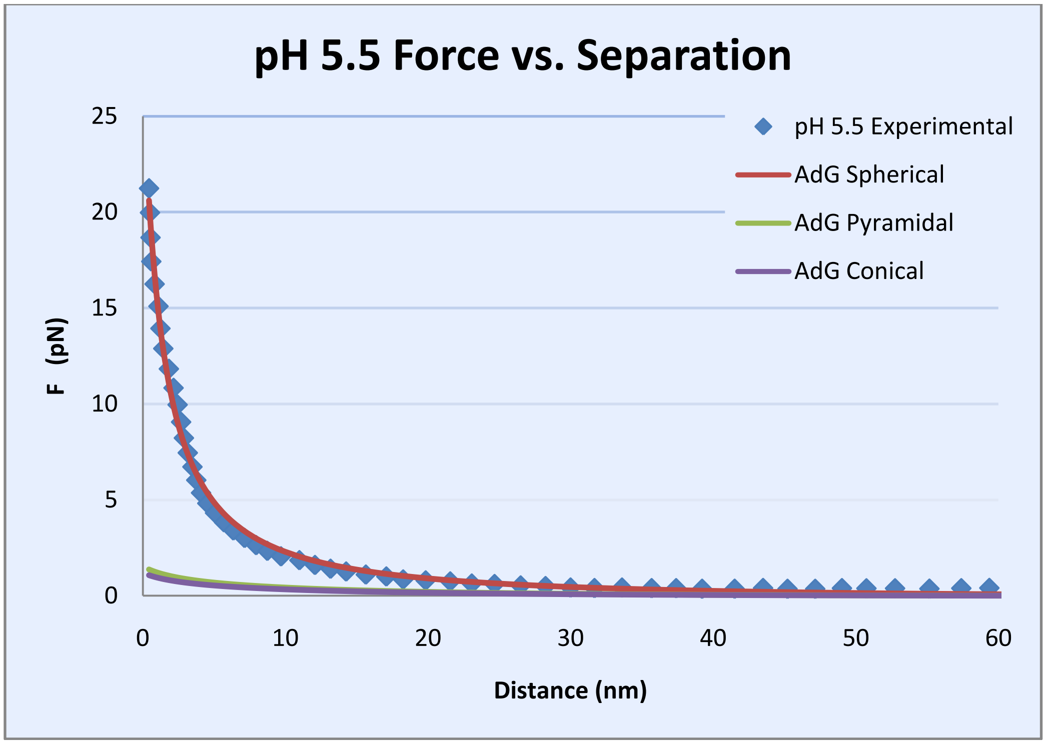

Figure 6-6 – Table Curve pH 5.5 force vs. separation plot used to fit model to data. The parameters obtained by this fit are 75.8, 97.5, and 1.8 nm for s, L, and h. The standard deviation percent error is 78%

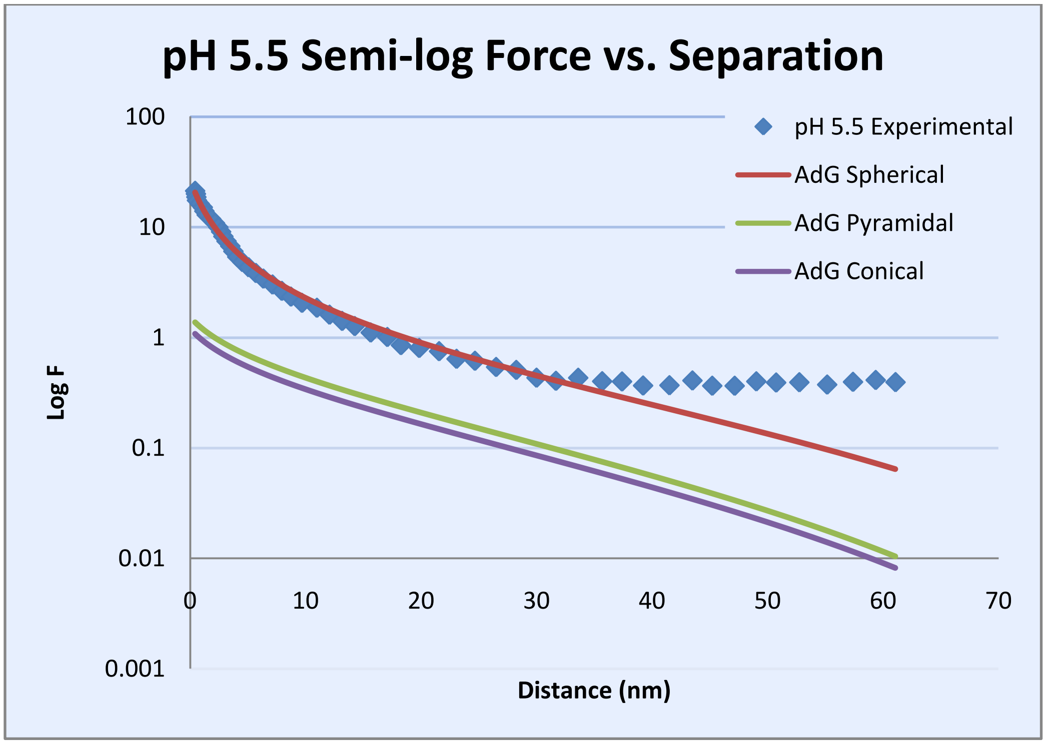

Figure 6-7 – Table Curve pH 5.5 semi-log force vs. separation plot used to fit model to data. The parameters obtained by this fit are 75.8, 97.5, and 1.8 nm for s, L, and h. The standard deviation percent error is 78%.

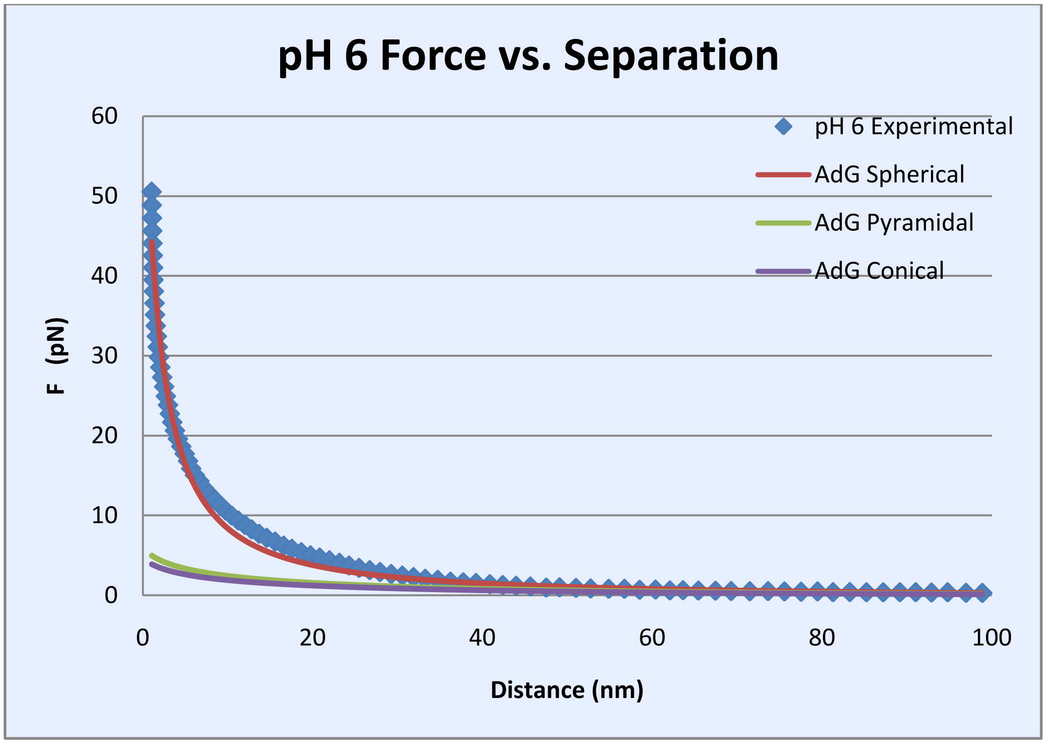

Figure 6-8 – Table Curve pH 6 force vs. separation plot used to fit model to data. The parameters obtained by this fit are 98.6, 243, and 2.3 nm for s, L, and h. The standard deviation percent error is 12%.

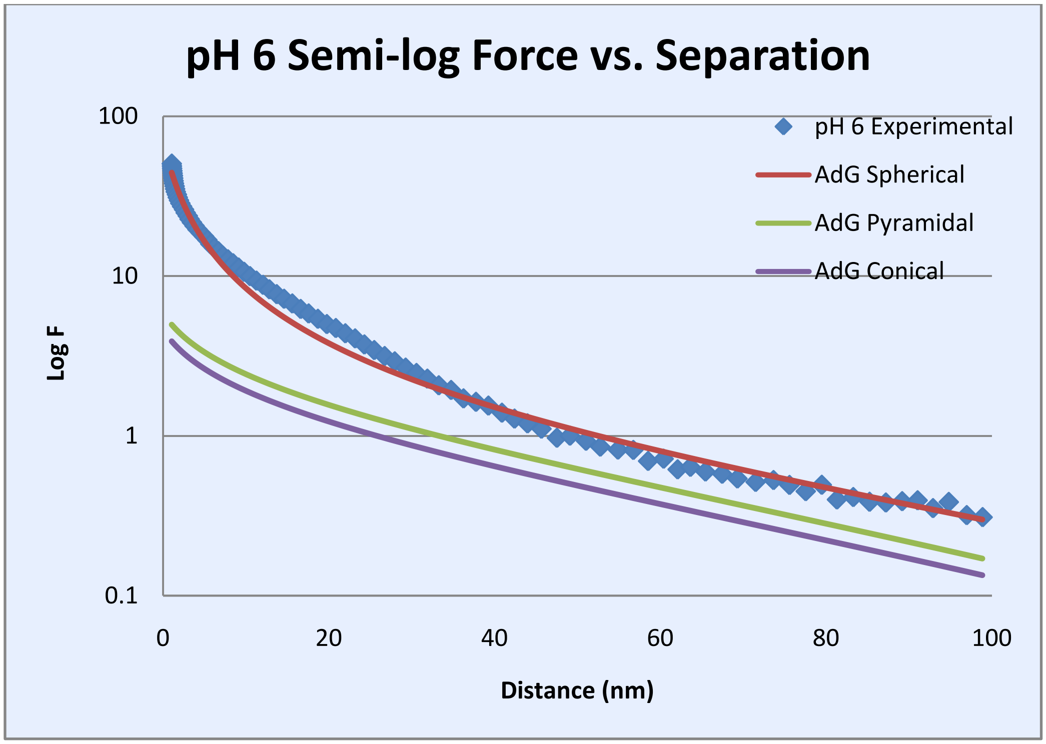

Figure 6-9 – Table Curve pH 6 semi-log force vs. separation plot used to fit model to data. The parameters obtained by this fit are 98.6, 243, and 2.3 nm for s, L, and h. The standard deviation percent error is 12%.

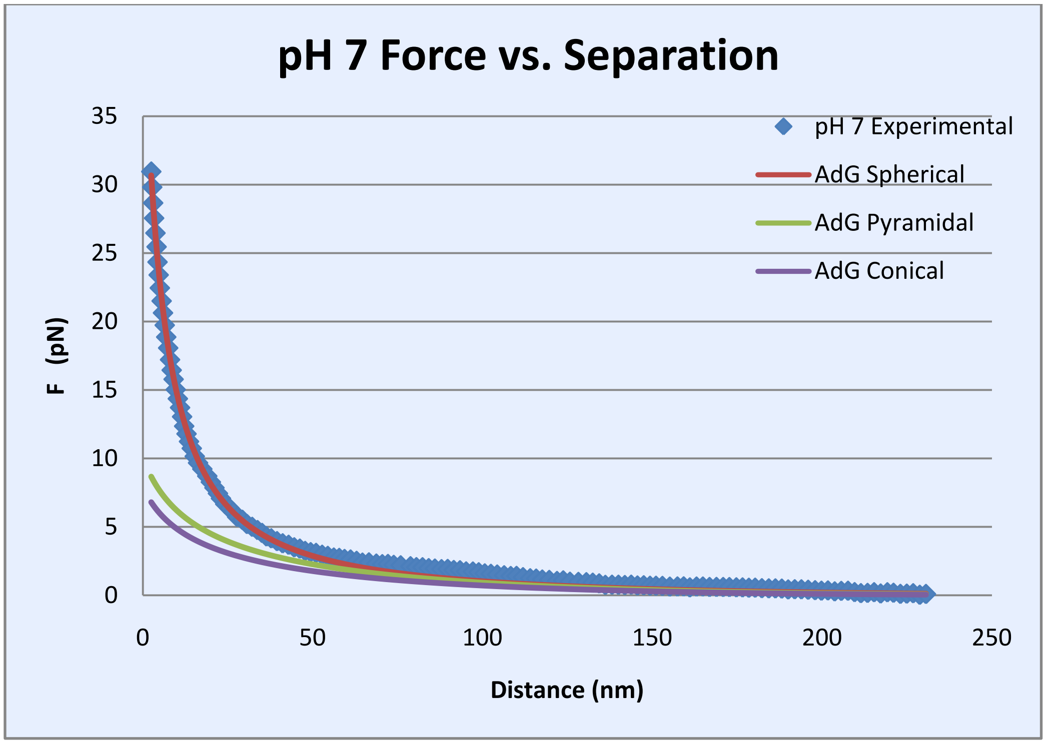

Figure 6-10 – Table Curve pH 7 force vs. separation plot used to fit model to data. The parameters obtained by this fit are 95.8, 364, and 7.35 nm for s, L, and h. The standard deviation percent error is 50%.

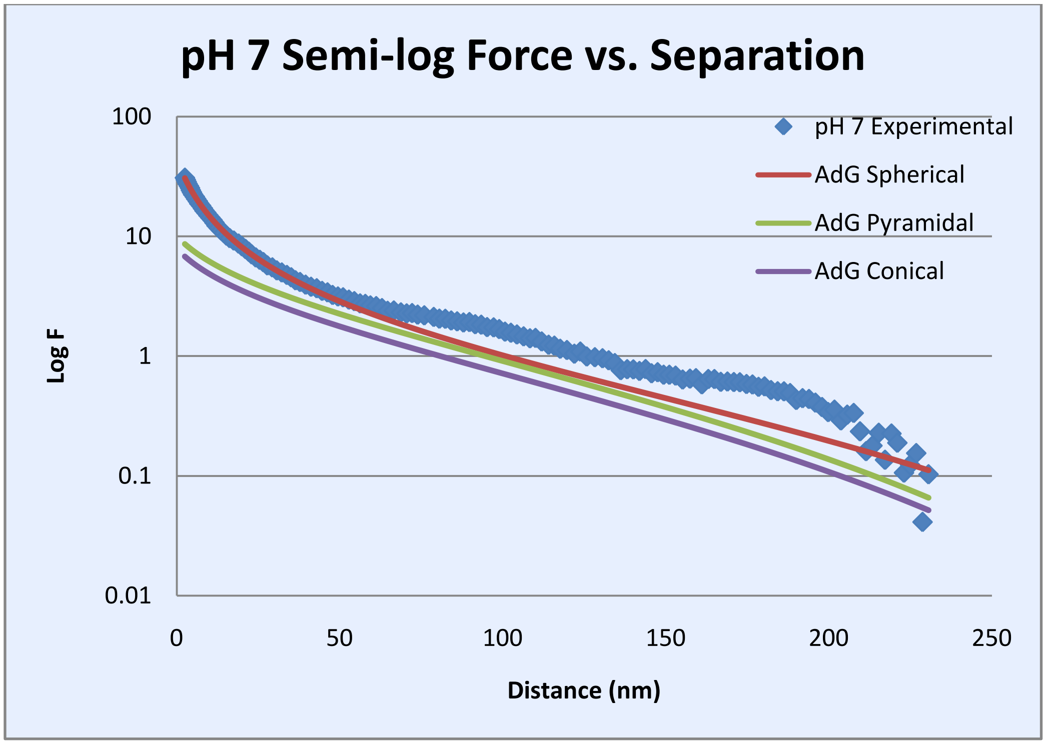

Figure 6-11 – Table Curve pH 7 semi-log force vs. separation plot used to fit model to data. The parameters obtained by this fit are 95.8, 364, and 7.35 nm for s, L, and h. The standard deviation percent error is 50%.

Table 6-1 – Summary of Results for Table Curve Fitting.

(nm)	**pH 5.5**	**pH 6**	**pH 7**
s	75.8	98.6	95.8
L	97.5	243	364
h	1.8	2.3	7.35
Std Deviation %	78	12	50

Table Curve produced the parameters shown in Table 6-1. A large error is observed if the same percentage standard deviation calculation from the Excel fitting is used, with the exception of pH 6 which produced a remarkably small error. The average percentage standard deviation in this case was 46.7%. This is an unacceptably large average error using this method of error minimization. The parameter trends seemed to make sense except for the value for *s* in pH 7 which decreased slightly from the previous condition. It is unclear if this is a result of fitting error due to problems with the data, or with the fitting itself. One way to fix this would be to have more trial data to fit.

6.4.1 Comparison of Fits

Table 6-2 – Comparison of Excel and Table Curve (TC) parameters.

(nm)	pH 5.5		pH 6		pH 7	
	TC	*Excel*	*TC*	*Excel*	*TC*	*Excel*
h	1.8	1.8	2.3	3.85	7.35	10
L	97.5	140	243	300	364	475
s	75.8	90	98.6	100	95.8	110
Std Dev	78	24	12	23	50	18

Table 6-2 compares the parameters obtained from fitting in Excel and Table Curve. In general, Excel produced a significantly lower percentage standard deviation, but this is because it was the specific error minimized to fit the data. Table Curve uses some sort of root-means-square method to fit the data, but this was not available for inspection or editing within the program. It was also not very thoroughly investigated due to time constraints. It is possible that Table Curve uses a superior fitting method that was just not considered.

Table Curve and Excel did seem to generally agree in trends, with the exception of how *s* behaves as a function of pH. However, the *s* value that Table Curve produced for pH 7 only differed slightly from pH 6. This could imply that some sort of error was encountered with either the fitting, or actual data of pH 7. It is also possible that the error was actually in both of the other pH conditions, because the error observed in pH 6 is drastically smaller than in the aforementioned. This suggests that something is different in the pH 6 data or fitting than the others.

Excel was ultimately chosen as providing the best fit for the data because of the problems with the larger error observed in Table Curve fitting. Excel also presented results that agreed with the original presumptions of the experiment, while Table Curve did not.

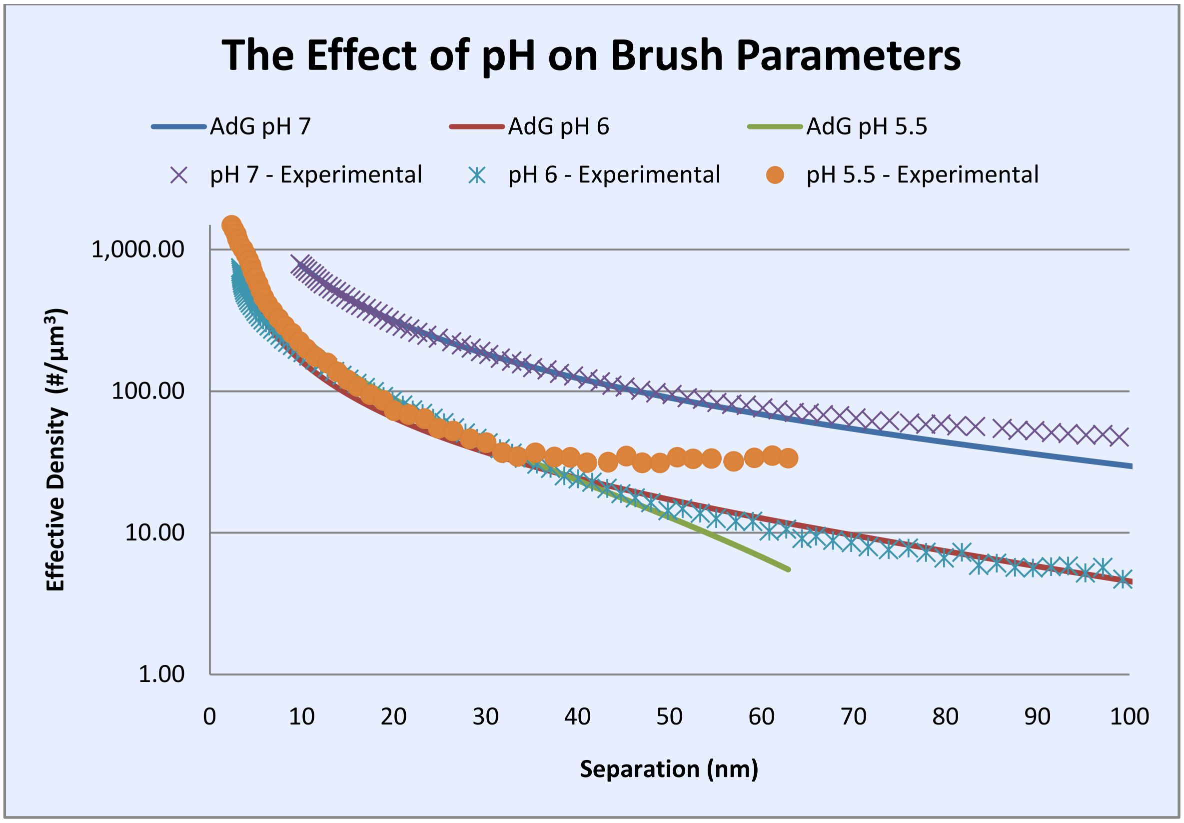

Figure 6-12 – Table Curve effective density plot demonstrating how brush parameters change with pH.